Micropore-Forming Gelatin Methacryloyl (GelMA) Bioink Toolbox 2.0: Designable Tunability and Adaptability for 3D Bioprinting Applications

Sili Yi, Qiong Liu, Zeyu Luo, Jacqueline Jialu He, Hui-Lin Ma, Wanlu Li, Di Wang, Cuiping Zhou, Carlos Ezio Garciamendez, Linxi Hou, Jin Zhang, Yu Shrike Zhang*

Dr. S. Yi, Dr. Q. Liu, Z Luo, J. J. He, H.-L. Ma, W. Li, D. Wang, Dr. C. Zhou, C. E. Garciamendez, Prof. Y. S. Zhang
Division of Engineering in Medicine
Department of Medicine
Brigham and Women's Hospital
Harvard Medical School
Cambridge, MA 02139, USA
E-mail: yszhang@research.bwh.harvard.edu

Dr. S. Yi, Prof. L. Hou, Prof. J. Zhang
College of Chemical Engineering
Fuzhou University
Fuzhou 350108, P.R. China

Abstract

It is well-known that tissue engineering scaffolds that feature highly interconnected and size-adjustable micropores are oftentimes desired to promote cellular viability, motility, and functions. Unfortunately, the ability of precise control over the microporous structures within bioinks in a cytocompatible manner for applications in 3D bioprinting, is generally lacking, until we recently reported a method of micropore-forming bioink based on gelatin methacryloyl (GelMA). This bioink took advantage of the unique aqueous two-phase emulsion (ATPE) system, where poly(ethylene oxide) (PEO) droplets were utilized as the porogen. Considering the limitations associated with this very initial demonstration, here we have furthered our understanding of the micropore-forming GelMA bioinks by conducting a systematic investigation into the additional GelMA types (porcine and fish, different methacryloyl-modification degrees) and porogen types (PEO, poly(vinyl alcohol), and dextran), as well as the effects of the porogen concentrations and molecular weights on the properties of our GelMA-based ATPE bioink system. We exemplify not only the significantly wider range of micropore sizes achievable and better emulsion stability, but also the improved suitability for both extrusion and digital light processing bioprinting with favorable cellular responses.

Keywords: poly(ethylene oxide) (PEO); poly(vinyl alcohol) (PVA); dextran; biofabrication; additive manufacturing; regenerative medicine

1. Introduction

Highly tunable and functional three-dimensional (3D) tissue scaffolds with tailored performances are meaningful to tissue engineering and regenerative medicine applications.[1, 2] Among the different biomaterials targeted towards scaffold fabrication, biocompatible hydrogels are considered as appealing candidates due to their cell-friendly aqueous environments as well as suitable structural and mechanical properties similar with most of the natural tissues.[3] In particular, volumetric hydrogel scaffolds with highly interconnected microscale porosities are more desirable for the transport of nutrients and oxygen, providing sufficient spaces for cell growth, attachment, and proliferation, as well as promoting cell-cell interactions over their non-microporous counterparts.[4]

To this end, the microporous structure is a critical parameter determining the performance of hydrogel scaffolds.[5] The microporous size, microporosity, and micropore interconnectivity of a construct provide essential cues that not only affect its physicochemical performances but also regulate cellular behaviors and functions.[6-8] In general, a highly microporous scaffold provides less diffusional resistance for oxygen, nutrients, and waste products, yet it may also result in insufficient structural mechanics and cellular interactions.[9, 10] Furthermore, previous reports have shown that different cell types may require scaffolds with different microporous sizes for maximum tissue growth, with the optimal average pore size ranging from a few to hundreds of micrometers.[11, 12] Although these size ranges may also be biomaterial-dependent, knowledge has accumulated suggesting the same importance of fabricating 3D cell-laden hydrogel scaffolds with appropriate microporous sizes and highly interconnected micropores, for applications targeted towards tissue (model) engineering and regenerative medicine.[3]

In recent years, 3D bioprinting has emerged as a collection of promising techniques for the fabrication of tissue constructs at high precision and accuracy, creating intricate biomimetic volumetric structures not conveniently achievable with traditional biofabrication methods.[13-16] Unfortunately, the ability of precisely controlling the microporous structures within hydrogel bioinks in a cytocompatible manner that can be adopted for various 3D bioprinting modalities, is generally lacking. One excellent demonstration showcased the utilization of a microbubble-generating device for the creation of microporous hydrogel matrices with extrusion bioprinting,[17] yet its translation to other bioprinting modalities and direct encapsulation of living cells during bioprinting may not be straightforward. Therefore, developing highly tunable micropore-forming

hydrogel bioinks that are simultaneously cytocompatible and widely applicable, is still in dire desire.

The aqueous two-phase system (ATPS) is a phase-separation phenomenon in a mixture of two hydrophilic phase-forming components at the critical concentrations.[18, 19] Recently, ATPSs have been recognized for their applications in extraction, separation, purification, and enrichment of biomolecules and cells, and has received intense attention in biomedical applications.[20, 21] Aside from its huge potential in these fields, ATPS can also form aqueous two-phase emulsions (ATPEs) by liquid-liquid phase-separation due to thermodynamic incompatibility between the two hydrophilic non-oppositely charged phases.[22-24] In the ATPE system, the compound with the ability of gelation is typically used as the continuous phase and the other without the gelling ability is used as the dispersion phase, where the emulsion droplets can be turned into interconnected microscale pores by selective removal after the continuous phase is crosslinked, so as to prepare microporous hydrogel constructs. Compared with conventional emulsions that rely on the incorporation of the organic phases or surfactants as porogens,[25] which are usually biologically toxic, the ATPE system can maintain a fully aqueous environment and exhibit excellent cytocompatibility allowing simultaneous cellular embedment, because the thermodynamic incompatibility between the aqueous solutions of certain water-soluble polymers necessitates no requirement of surfactants, particulate stabilizers, or organic solvents.[26, 27]

We pioneered the invention of ATPE-enabled micropore-forming bioinks by mixing poly(ethylene oxide) (PEO, MW: 3×10^5 Da) aqueous solution with gelatin methacryloyl (GelMA) aqueous solution for the preparation of hierarchically microporous cell-laden hydrogel constructs via 3D bioprinting.[28-30] However, numerous challenges still remain to be overcome in this initial version of the micropore-forming GelMA bioink of ours, such as the tunability of the micropore size, the emulsion stability, and the bioprinting performance. Herein, a series of bioinks based on ATPE have been further developed, which we term as the 'micropore-forming GelMA bioink toolbox 2.0', with wide tunability and adaptability for tissue biofabrication using both extrusion bioprinting and digital light processing (DLP) bioprinting (**Figure 1**). The effects of the composition of the ATPE bioink, such as continuous-phase GelMA type and their concentration, as well as dispersion-phase compound type, molecular weight, and concentration, on the bioink performances, were systematically studied with phase diagrams plotted accordingly. It is of significance that we can now, precisely endow the bioprinted GelMA hydrogel constructs with

designable properties using our micropore-forming bioink toolbox 2.0. It is believed that our unique bioinks would pave new avenues for advanced tissue bioprinting in the future.

2. Experimental Section

2.1. Materials

Unless otherwise noted, all chemicals and reagents were purchased from Sigma-Aldrich (USA) and used without further purification. Dextran was purchased from Aladin (China), lithium phenyl-(2,4,6-trimethylbenzoyl) phosphinate (LAP) was purchased from Allevi (USA), and Ruthenium Visible Light Photoinitiator was obtained from Advanced BioMatrix (USA). Live/Dead™ Viability/Cytotoxicity Kit, PrestoBlue® cell viability reagent, Alexa® 488-phalloidin, 4',6-diamidino-2-phenylindole (DAPI), and permeabilization buffer were purchased from ThermoFisher (USA). Syringe filters (0.22 μm in pore size) were purchased from VWR International (USA).

2.2. Preparation of GelMA bioinks and hydrogels

GelMA were synthesized as described previously.[31-33] Briefly, type-A porcine skin gelatin or fish skin gelatin (10 g) was dissolved in Dulbecco's phosphate-buffered saline (DPBS) by stirring at 50 °C to produce a uniform gelatin solution (10 wt.%). Then, methacrylic anhydride (MA) was added to the gelatin solution at a rate of 0.5 mL min^{-1} to react for 3 h at 50 °C under vigorous stirring. Final concentration of MA was 1 wt.%, 5 wt.%, or 8 wt.%, respectively, referred to herein as Low-, Medium-, or High-GelMA. The reaction was stopped by 5-time dilution with warm DPBS, and unreacted MA and additional by-products were removed through dialysis in deionized water at 50 °C for 7 days using 12–14 kDa MW cut-off membranes. The white foamy GelMA was then obtained by lyophilizing the solution.

For the preparation of the micropore-forming bioink, the lyophilized GelMA containing the photoinitiator, and the porogen, were separately dissolved in DPBS at 50 °C at the desired concentrations, to prepare the GelMA pre-gel solution and the porogen solution, respectively. They were also filtered by 0.22-μm filters as necessary. Subsequently, the GelMA pre-gel solution and the porogen solution were mixed thoroughly with a pipette to form the micropore-forming bioink.

For the preparation of the micropore-forming GelMA bioink, LAP powder (0.5 wt./vol.%) was mixed thoroughly with the bioink formulated with intended combination of GelMA and

porogen, by pipetting (<1 mL) or vortexing (>1 mL; 500-1,000 rpm) for 5 s, resulting in formation of the pre-gel emulsion. For tests based on bulk hydrogels, the emulsions were filled into polydimethylsiloxane (PDMS) molds and crosslinked with a UV lamp (λ = 365 nm, 0.5 W cm^{-2}, OmniCure S2000, Excelitas Technologies, Canada) for 30 s to form the hydrogel constructs. The porogens are subsequently leached out by immersing the constructs in DPBS, as we previously reported.[28]

2.3. Characterizations

2.3.1. Microscopic observations: The microporous structures of the GelMA hydrogels were captured by an inverted fluorescence microscope (Zeiss Axio observer D1, Carl Zeiss, Germany).

2.3.2. Porosity measurements: A liquid-displacement method was used to measure the microscale porosities of the GelMA hydrogels formed by the ATPE, but not the nanoscale pores present in between the polymer chains within the GelMA phase. Therefore, the microscale porosities were calculated based on the porosities of the corresponding pure GelMA hydrogels set to '0' in the same aqueous environment. Briefly, the same-sized non-microporous and microporous GelMA hydrogel samples were immersed in deionized water overnight and weighed after removing the excess water on the hydrogel surfaces. The microscale porosity was determined using the following Equation (1):

$$\text{Porosity} = (M_2\text{-}M_1)/\rho V \quad (1)$$

, where M_1 is the mass of the non-microporous GelMA hydrogel sample after immersion in deionized water, M_2 is the mass of the microporous GelMA hydrogel sample after immersion in deionized water, ρ is the density of the water, and V is the volume of the sample.

2.3.3. Swelling ratio measurements: The samples were incubated in DPBS for 24 h at 37 °C, taken out from DPBS, lightly blot-dried and weighed. The samples were then freeze-dried for 24 h and weighed to determine the dry masses. The swelling ratio of the swollen gel was calculated according to Equation (2):

$$\text{Swelling ratio} = (W_S\text{-}W_D)/W_D \times 100\% \quad (2)$$

, where W_S is the mass of the GelMA hydrogel sample after incubated in DPBS, W_D is the mass of the GelMA hydrogel sample after freeze-drying.

2.3.4. Rheological measurements: The rheological properties of the various bioinks were evaluated on a physical MCR 302 rheometer (Anton-Paar, Austria) using parallel plates (PP25) with zero gap fixed at 0.5 mm. The viscosity values of the bioinks were measured from 2-40 °C at the shear rate of 10 s^{-1}. The apparent shear viscosity values were monitored by shear tests, where the shear rate ranged from 0.01 s^{-1} to 100 s^{-1}, which is deemed to be within the range commonly used for extrusion bioprinting.[28, 34]

2.3.5. Mechanical property evaluations: The mechanical properties of the photocrosslinked GelMA constructs (cylinder, 10 mm in diameter and 2 mm in thickness) were measured by compression tests using a mechanical testing machine (Instron, USA) at room temperature. The compression was applied at a rate of 0.5 mm min^{-1} in a range of 0-50% strain. The compressive modulus was determined from the slope of the linear portion of the stress-strain curve corresponding to 0-10% strain range.

2.4. Cell culture

NIH/3T3 fibroblasts and HepG2 hepatocellular carcinoma cells were purchased from ATCC (USA). Both cells were cultured in Dulbecco's modified Eagle medium (DMEM) supplemented with 10 vol.% fetal bovine serum (FBS) and 1 vol.% penicillin-streptomycin (all from ThermoFisher) at 37 °C in a standard incubator at 100% humidity and 5% CO_2. The culture medium was replaced every 2-3 days and the cells were passaged approximately twice per week.

2.5. Bioprinting

The cell density in the micropore-forming bioink used for bioprinting was 1×10^6 cells mL^{-1}. Extrusion bioprinting was performed using a commercial bioprinter (Allevi 2, Allevi). The bioink (2 mL), cell-free or cell-laden and using LAP (0.5%) as the photoinitiator, was filled into a syringe (10 mL), followed by cooling at 4 °C for 20 min. The bioprinting parameters were set as follows: the final GelMA concentration at 5-20 wt.%, the final porogen concentration at 0-5 wt.%, extrusion pressure at 0-60 psi, syringe temperature: 15-25 °C, and nozzle inner diameter of 0.2 mm (27G) or 0.25 mm (25G). For bioprinted cell-laden constructs, 30 s of UV exposure (λ = 365 nm, 0.5 W cm^{-2}) was used for crosslinking and they were subsequently incubated in culture medium at 37 °C

and 5% CO_2 for culture.

DLP bioprinting was performed using a custom-built bioprinting system.[35-37] The system consisted of a visible-light LED source, a digital micromirror device (DMD) chip, a set of lenses and mirrors, and a controller software, assembled in an inverted format. For a typical fabrication process, the bioink in the vat was photocrosslinked layer-by-layer with defined patterns at a light intensity of 0.5 W cm^{-2} and a layer thickness of 150 μm. Also different from extrusion bioprinting, the bioink here used ruthenium III (Ru, 2 mM)/sodium persulfate (SPS, 20 mM) as the photoinitiator,[38] which also contained a photoabsorber (food dye) at 2%. Following bioprinting, the cell-laden constructs were subsequently incubated in culture medium at 37 °C and 5% CO_2 for culture.

2.6. Cellular assays

Cell viability was determined by Live/Dead assay according to the manufacturer's instructions. Briefly, cell-laden hydrogel constructs were stained with calcein AM (0.5 μL mL^{-1}, green) and ethidium homodimer-1 (2 μL mL^{-1}, red) for 25 min, and then observed under an inverted fluorescence microscope (Nikon, Japan). Cell viability was quantified by counting live and dead cell numbers using Fiji ImageJ software.

Cell proliferations were quantified using PrestoBlue® reagent in cell culture medium. Cell-laden hydrogel constructs were washed with DPBS and added with the PrestoBlue solution (10 vol.%), followed by incubation at 37 °C and 5% CO_2 for 4 h. Then, 200-μL supernatant from each well was collected for fluorescence measurement at 560/590 nm (excitation/emission) with a spectrophotometer (Bio-Tek Instruments, USA). In addition, F-actin and nuclei staining (phalloidin/DAPI) were used to observe cell spreading. Cell-laden hydrogel constructs were treated with a fixed solution (3.7% paraformaldehyde in PBS, pH = 7.0) for 30 min. The fixed constructs were stained for F-actin and nuclei with Alexa 488-phalloidin solution (100 nmol L^{-1}) and DAPI solution (100 nmol L^{-1}), respectively. The fixed constructs were washed with PBS and then observed under an inverted fluorescence microscope (Nikon).

2.7. Statistical analyses

Single comparisons were assessed via t-tests, and one-way ANOVA was used for multiple comparisons, performed in IBM® SPSS® Statistics software (USA). The statistical significance

was determined at *p<0.05, **p<0.01, and ***p<0.001. At least triplicates were used for all analyses.

3. Results and Discussions

First, six different GelMA types were synthesized by the reaction of type-A porcine skin gelatin or fish skin gelatin with different concentrations of methacrylic anhydrate (1%, 5%, and 8% (v/v) according to our previously published procedures.[31-33] These different formulations are referred to herein as Low-Porcine-GelMA (LP-GelMA), Low-Fish-GelMA (LF-GelMA), Medium-Porcine-GelMA (MP-GelMA), Medium-Fish-GelMA (MF-GelMA), High-Porcine-GelMA (HP-GelMA), and High-Fish-GelMA (HF-GelMA). Studies have shown that gelatins derived from different sources offer unique material properties.[39, 40] For example, bovine and porcine gelatins have higher tensile strengths and percent elongation values compared to fish gelatin. Fish gelatin has a much lower gelation temperature than those of other species due to fish gelatin having lower concentrations of proline and hydroxyproline. Therefore, different gelatin types may suit for different bioprinting applications. Next, three water-soluble polymers, including PEO, PVA, or dextran with different molecular weights, were employed as the dispersion phase in the continuous GelMA phase, to investigate whether the concentration and molecular weight of the dispersion phase, as well as the GelMA type could have an impact on the formation of microporous GelMA hydrogels. The experimental procedure is schematically illustrated in **Figure 2a**.

Thermodynamically, the phase-separation of an aqueous mixture occurs when the entropic contribution that favors mixing becomes smaller relative to the enthalpic penalty that opposes it.[41] Therefore, when the GelMA continuous phase and the dispersion phase are both at lower concentrations, their aqueous mixture would form a single phase resulting in the absence of emulsion droplets. With the increase in the concentration of the dispersion phase, the aqueous mixture would then spontaneously phase-separate into two immiscible phases due to the molecules coming close and increasing the free-energy level, where the GelMA continuous phase is then solidified to form a hydrogel containing the emulsion droplets of the dispersion phase, which acts as the porogen to guide pore-formation after GelMA photocrosslinking. However, if the degree of phase-separation, as increased with the elevation of the dispersion-phase concentration, further continues beyond a point, the GelMA continuous phase becomes difficult to be crosslinked

anymore as an entirety.

We arbitrarily defined the concentration of the dispersion phase required for the formation of micropores (i.e., the microscale pores formed by the ATPE but not the nanoscale pores present in between the polymer chains) in the GelMA hydrogels to be larger than 10 μm as the critical concentration, since smaller pores are typically not desirable for our intended applications. The ternary phase diagrams of the various GelMA and porogen types are shown in **Figure 2b**, which reveal the concentration thresholds for the components involved in the formations of the ATPEs, for each GelMA/porogen combination. These ternary phase diagrams suggested that the concentration range for the preparation of the micropore-forming GelMA bioinks was closely related to not only the concentration and type (porcine/fish, degree of methacryloyl-modification) of GelMA used, but also more critically, the concentration, molecular weight, and type of the porogen selected. For a single type of the porogen, the higher the molecular weight, the lower the critical concentration for micropore-formation in the GelMA phase was required; at the meantime, the concentrations that inhibited the proper crosslinking of the continuous GelMA phase were also lower across the different GelMA types. The possible reason is that the higher molecular weight the porogen is, the easier it is to aggregate, forming larger emulsion droplets due to the higher hydrophobicity of polymer chains and the larger hydrodynamic radius, and resulting in improved phase-separation.[23, 42] As far as the PEO, PVA, and dextran porogen materials with the same molecular weight (e.g., 1×10^5 Da) were concerned, the critical concentrations for the micropore-formation exhibited significant differences (**Figure S1**), which might be cause by their different interfacial characteristics inducing the differences in thermodynamic properties of incompatible solutions, which further affect the tendency of solution phase separation.[43, 44] For the same GelMA origin (either porcine or fish), the higher the degree of methacryloyl-substitution, the smaller concentration of the dispersion phase was required to form the emulsion. Overall, the impact of the type of GelMA on ATPE-formation was deemed inferior compared to the porogen parameters.

Based on the phase diagrams (**Figure 2b**), we further investigated the sizes of the micropores in the resulting hydrogel constructs made of MP-GelMA (10 wt.%) and porogen (PEO: 1 wt.%; PVA: 2 wt.%; or dextran: 2 wt.%; concentration chosen based on the mid-range for each porogen type). The resulting microporous MP-GelMA hydrogel constructs following GelMA photocrosslinking and porogen-removal were imaged under a microscope (**Figure 3a**). It was clear

that, when the MP-GelMA and the porogen concentrations were kept constant, the average size of the micropores increased and the micropore distribution became broader as the molecular weight of the porogen was elevated, for PEO, PVA, or dextran. The quantitative analyses of size distributions of the micropores in the MP-GelMA hydrogel constructs were further derived by measuring 100 individual pores directly from optical microscopic images (**Figure S2**). Using PEO, PVA, or dextran as the porogen, the average size of the micropores was enhanced from 7.2 ± 1 μm, 10.6 ± 2.2 μm, or 3.6 ± 1.8 μm to 49 ± 3.2 μm, 42 ± 3.0 μm, or 40 ± 3.1 μm, respectively, with the increased the molecular weight of the corresponding porogen.

The effects of PEO, PVA, and dextran with the same molecular weight (1×10^5 Da) on the pores size of the GelMA hydrogels were also investigated. The micropore sizes of the MP-GelMA hydrogel constructs gradually increased with the increase of the porogen concentrations (**Figures S3a and S4**), for GelMA concentrations at both 5 wt.% and 10 wt.%. At the same concentrations of the porogens, the pores size of the GelMA hydrogel constructs prepared with PEO as the porogen was the largest, even though the continuous phase featured different GelMA types (**Figure S3b**). In addition, as the degree of methacryloyl-modification was elevated, the water solubility of GelMA gradually decreased, the pores size of the hydrogel constructs made of GelMA (10 wt.%) and dextran (2 wt.%, MW: 5×10^5 Da) increased from 16.2 ± 2 μm to 26 ± 2.2 μm (**Figure S5**). Collectively, the types of the GelMA continuous phase and the porogen dispersion phase, as well as the molecular weight and concentration of the latter, were found to affect the micropore size of the prepared GelMA hydrogels, providing us with a versatile toolbox of the micropore-forming GelMA bioinks with a broad range of designable micropore sizes to select from. Confocal 3D reconstruction views of a typical microporous MP-GelMA hydrogel construct made of MP-GelMA (10 wt.%) and PVA (2 wt.%, MW: 1×10^5 Da) are illustrated in **Figure 3b**, where the interconnected microporous structure within the construct was obvious. It should be noted that, once the continuous-phase GelMA is crosslinked, the structure would stay stable, and their morphological changes should only subject to excessive external forces or degradation.

Next, a range of physical properties of the microporous GelMA hydrogels were characterized to understand their performances. For example, we used MP-GelMA as the continuous phase and PVA (MW: 1×10^5 Da) as the porogen, investigating the swelling ratios and the porosities of the resulting microporous hydrogel constructs, which have been shown to effectively affect the cellular microenvironments.[45] Previous studies indicated that increased GelMA concentration

would result in a reduced swelling ratio due to the increased crosslinking density.[46] In our case, increasing the PVA concentration of the micropore-forming MP-GelMA (10 wt.%) bioinks from 0 wt.% to 3 wt.%, the micropore size of the MP-GelMA hydrogels gradually increased resulting in an increased swelling ratio from 10% to 16% (**Figure 3c**). This observation was likely due to the fact that with the elevation of the PVA concentration, the microscale porosity of the GelMA hydrogel increased from 0% to 56% (**Figure 3d**), effectively reducing the collective crosslinking densities of the constructs. The crosslinking densities of the GelMA backbones, however, should not differ significantly with those in pure GelMA hydrogels crosslinked under similar conditions. The results have suggested that the swelling ratio and microscale porosity of the microporous GelMA hydrogel constructs could be readily tuned by varying the porogen concentration.

We further used PVA (MW: 1×10^5 Da) as the porogen as an example to evaluate the mechanical behaviors of the resulting microporous GelMA hydrogel constructs (after porogen was removed), in the compression mode with varying GelMA types and concentrations. The compressive modulus was determined from the slope of the linear portion of the stress-strain curve (ε: 0-0.1).[47] It was found that the compressive moduli of the microporous hydrogel constructs gradually decreased with the change of the concentration of PVA in the micropore-forming bioink from low to high (**Figure 3e-f**), caused by the increase in the micropore sizes of the hydrogels. The data also illustrated the positive correlation between the GelMA concentration and the compressive modulus, ranging from <5 kPa at 5% MP-GelMA to ca. 90 kPa at 20% MP-GelMA (**Figure S6a, b**), likely caused by an increased crosslinking density at the higher GelMA concentrations. Moreover, the microporous porcine GelMA hydrogels were stiffer than those made of fish GelMA at the same degrees of methacryloyl-modification (**Figure S6c, d**). Collectively, the micropore size (as determined primarily by the concentration of the dispersion phase) as well as the concentration and the degree of methacryloyl-functionalization of GelMA, along with their type (porcine or fish), all impact the mechanical properties of the resultant microporous GelMA hydrogels. It should be noted that, although we did not examine the mechanical performances of microporous GelMA hydrogels produced with other porogen types, we anticipate them to show a similar trend in such relations. Therefore, we were able to engineer with precision, the properties of these hydrogels to potentially target specific tissues of interest.

Benefiting from an abundance of integrin-binding motifs and matrix metalloproteinase-sensitive groups that can promote cell adhesion and motility despite their cost-effectiveness,

GelMA hydrogels are particularly attractive as tissue scaffolds.[48] In this work, two commonly used cell types, the NIH/3T3 mouse embryonic fibroblasts and the HepG2 human liver-like cells were chosen as representative models to further showcase the biological performances of our micropore-forming GelMA bioink toolbox 2.0.

Since the dispersion phase functions as a key component of the micropore-forming bioinks, which are also co-existent with the encapsulated cells in the GelMA continuous phase prior to GelMA crosslinking and porogen-removal, we investigated the cytotoxicity of the dispersion-phase materials (PEO, PVA, and dextran). The relevant cell viability results are shown in **Figure S7**. It was pleasantly clear that all of the dispersion-phase materials exhibited low cytotoxicity levels even though their concentrations were as high as 4 wt.% in the micropore-forming bioinks. Then, we used micropore-forming bioinks with GelMA as the continuous phase and PVA (MW: 1×10^5 Da) as the dispersion phase to prepare the microporous GelMA hydrogel constructs for more in-depth assessments of cell activity, proliferation, and spreading/aggregation. Cells encapsulated within the pure (non-microporous) GelMA hydrogels were used as the controls. Consistent with **Figure S7**, both cell types indicated good viability in all types of HF-GelMA hydrogels after 7 days of cultivation (**Figure 4a, b**). In comparison, the NIH/3T3 fibroblasts exhibited lower viability in the hydrogels made of 10 wt.% MP-GelMA than that of same cells in hydrogels made of 5 wt.% MP-GelMA, even though both were microporous, possibly due to the low cell adaptability to the stiff GelMA hydrogel backbones (**Figure S8**).

Interesting, while the HepG2 cells also exhibited a lower viability in the non-microporous MP-GelMA (10 wt.%) hydrogels, a significantly higher viability for them in the microporous MP-GelMA hydrogels at the same MP-GelMA concentration was observed, demonstrating that the presence of the micropores provided a suitable microenvironment for HepG2 growth. Cell proliferation profiles were simultaneously evaluated by the PrestoBlue® assay (**Figures 4c and S9**). The results indicated that in all cases the cell proliferations were enhanced in the microporous HF-GelMA hydrogels as compared with the non-microporous HF-GelMA hydrogels, since the cells inside the non-microporous GelMA hydrogels were restricted by the relatively dense polymer networks. Nonetheless, it was also found that for the NIH/3T3 fibroblasts, when the micropore size became too large (PVA: 2 wt.%), their proliferation became reduced unlike the HepG2 cells, perhaps due to the marked difference in the sizes between these two cell types, because different cells have been shown to require scaffolds of different pore size for maximum growth.[49-51]

We further evaluated the cell spreading in the microporous HF-GelMA hydrogels (**Figures 4d-e, S10, and S11, and Video S1**). Greater numbers of spreading NIH/3T3 fibroblasts were observed in the microporous HF-GelMA constructs in comparison to those in the non-microporous HF-GelMA constructs at both Day 3 and Day 7, with an exception at 2% PVA where the numbers seemed similar to the other groups at Day 3 and slightly lower at Day 7 (**Figures 4d-e and S10**), in line with the quantification results (**Figure S9**). It is worth noting that, very different from the spreading behaviors of the NIH/3T3 fibroblasts, the HepG2 cells displayed a true state of multicellular spheroid growth during 7-day culture period, indicating much more aggregate-formation with also larger sizes as the microscale porosity of the HF-GelMA hydrogels was increased (**Figures 4e and S11, and Video S1**). This observation is significant since it suggested that the microporous HF-GelMA hydrogels could potentially better-emulate the realistic cellular microenvironments leading to formation of liver (or liver cancer)-like tissues otherwise hard to achieve in conventional, non-microporous GelMA hydrogel constructs used at the same GelMA concentration. Of note, when using pure GelMA bioinks at lower concentrations, cellular behaviors may improve and approach those observed in our microporous GelMA hydrogels at higher GelMA concentrations, which however, may not be suited for extrusion bioprinting in the conventional setup.

Altogether, the experiments proved that the highly interconnected and microporous GelMA hydrogels formed by our unique micropore-forming bioink toolbox 2.0 were not merely cytocompatible but also able to provide spaces for the spreading or aggregation of the encapsulated cells compared to their non-microporous counterparts, in a cell type-dependent manner. Of note, considering the cytocompatible nature of PEO and dextran, we anticipate their combinations with GelMA would likely show a similar trend in retaining cellular viability and promoting cellular activities as we demonstrated here with PVA as the exemplary porogen. Therefore, it is possible to adjust the properties of the micropore-forming bioinks according to the target cell characteristics to meet the optimal needs for their growth.

In the subsequent sections, the wide adaptability of our micropore-forming GelMA bioink toolbox 2.0 is elaborated. Foremost, the rheological properties of a bioink are critical for its printability, especially for extrusion bioprinting. As such, the rheological behaviors of the micropore-forming bioinks were studied in terms of their various compositions. As well-known, GelMA is a temperature-sensitive material that experiences a gel-to-solution transition when the

temperature is elevated.[34] As a demonstration, we selected MP-GelMA as the continuous phase and PVA as the dispersion phase to measure the viscosity-temperature relationship of the micropore-forming bioinks. The results were aligned with our expectation, where all the bioink formulations had an obvious decrease in viscosity when the temperature was increased (**Figure 3g**). In particular, the concentration and molecular weight of PVA had obvious effects on the viscosity values of the bioinks at below 25 °C; the higher concentration or molecular weight resulted in the lower viscosity range. The viscosity-shear rate relationships of the micropore-forming GelMA bioinks with different compositions were subsequently investigated (**Figure S12**). The apparent shear-thinning behaviors were observed for all the bioink formulations within the shear rate range from 0.01 to 100 s^{-1} at 25 °C, under which temperature the bioinks exhibited a semi-solidified state (**Figure S12a-c**).[28-30] Increasing the GelMA concentration, decreasing the PVA concentration, or decreasing the PVA molecular weight, all led to an elevation of the viscosity values across the shear rate range tested. Furthermore, both the higher concentration of GelMA and the lower molecular weight of PVA created the higher-viscosity micropore-forming bioinks (**Figure S12d and e**).

Extrusion-based 3D bioprinting is perhaps the most extensively adopted modality in additive biomanufacturing over the last decade.[52] The versatility of this approach allows it to be compatible with a wide array of bioinks including cell-laden hydrogels, microcarriers, and scaffold-free cell aggregates.[53-55] While viscosity values provide some guidelines, the printability of our micropore-forming bioinks base on extrusion bioprinting was first systematically analyzed, where the effects of the compositions of the bioinks were examined. Previous studies have suggested that bioinks during extrusion bioprinting usually exhibit droplet-, filament-, or fractured morphology at the nozzle outlet.[56] Specifically, unstable bioinks usually form droplets, whereas over-gelled bioinks easily form fractured filaments. Therefore, only if smooth and uniform filaments were extruded continuously could it end up with the deposition of quality-patterns and constructs that are considered as suitable bioprinting performances.

Here we selected PVA as the porogen for demonstration purpose. In the case of lower degrees of methacryloyl-substitution of GelMA and higher concentrations of PVA, the bioinks formed spindle-shaped filaments, oftentimes even breaking to form droplets due to the longitudinal instability occurring at the nozzle outlet. However, in the case of excessively high concentrations of GelMA and very low concentrations or molecular weights of PVA, the bioinks on the other hand,

became too viscous leading to wrinkled filaments. Therefore, these formulations of the micropore-forming GelMA bioinks were considered as non-printable (white regions in **Figure 5a-c**). By adjusting the suitable type and concentration of GelMA, as well as concentration and molecular weight of PVA, the bioinks could steadily form smooth and uniform filaments. Thus, these regions were considered as printable (green regions in **Figure 5a-c**). It should be pointed out that, our micropore-forming GelMA bioink toolbox 2.0 provided significantly improved capacities in terms of adjustable rheological properties and other parameters over our initial version of the bioink solely based on a single type of GelMA (porecine) and a single type of porogen (PEO) with a single molecular weight (3×10^5 Da).[28-30]

Now knowing the printability range of our micropore-forming GelMA bioink toolbox, single-layer patterns and 3D structures were extrusion-bioprinted using the bioink made of HF-GelMA (10 wt.%) and PVA (1 wt.%, MW: 1×10^5 Da) as a demonstration (**Figure 5d**). These constructs included for example, a single-layered Harvard badge, a 5-layered Chinese knot with a size of ca. $10\times10\times2.5$ mm^3 (wall thickness: 0.8 mm), a 13-layered inverted cone with a size of ca. $10\times10\times6.5$ mm^3 with varying diameters along the height of 1 to 6.5 mm (wall thickness: 0.4 mm), a 10-layered mesh cube with a size of ca. $10\times10\times5$ mm^3 (wall thickness: 0.8 mm; strand distance: 1.5 mm), and a 10-layered thin-walled tube with a size of ca. $10\times10\times5$ mm^3 (wall thickness: 0.4 mm). Of note, similar 3D patterns were also successfully bioprinted using different compositions of the micropore-forming bioink (**Figure S13**). These results proved the favorable physical properties of our micropore-forming bioinks for reliable production of complex 3D hydrogel constructs with designable flexibility, using extrusion bioprinting.

We then investigated the cell viability and spreading in extrusion-bioprinted cell-laden GelMA hydrogel constructs (meshes with a size of ca. $10\times10\times2$ mm^3) using the same bioink made of HF-GelMA (10 wt.%) and PVA (1 wt.%, MW: 1×10^5 Da). Live/dead staining (**Figure 5e**) and quantification analyses (**Figure S14a**) revealed that both NIH/3T3 fibroblasts and HepG2 cells in the bioprinted constructs possessed high viabilities through the 7-day culture period. As also suggested in the F-actin staining images (**Figure 5f**), both cell types exhibited homogeneous distributions with significant spreading or aggregation of the cells over the culture period. Similar to the scaffolds formed by molding (**Figure 4d and e**), the NIH/3T3 fibroblasts and the HepG2 cells exhibited excellent spreading or aggregation in the bioprinted microporous GelMA hydrogel constructs (**Figure 5f**). Moreover, the structural integrity of the bioprinted hydrogel constructs was

faithfully maintained even after cell spreading/aggregation following 7 days of culture. Therefore, it is reasonable to argue that the extrusion bioprinting process did not significantly affect the cell activities, and the bioprinted patterns provided favorable geometrical, mechanical, and biological microenvironments for cell adhesion and growth.

More recently, light-based bioprinting techniques have been increasingly adopted due to their avoidance of shear stresses associated with the cell extrusion processes and that they are generally faster at higher resolutions, which are especially favorable characteristics in tissue biofabrication.[57-59] Herein, DLP bioprinting[35, 60] was employed to further illustrate the feasibility of our micropore-forming bioinks to create cell-laden microporous GelMA hydrogel constructs possessing various 2D patterns and 3D shapes with up to sub-100 μm-scale resolutions.

Unlike extrusion bioprinting where the GelMA-based bioinks (including our micropore-forming bioinks) could be pre-stored at a lower temperature (e.g., 4 °C) to first allow gelation to enable faithful bioprinting, the stability of the emulsions in the micropore-forming bioinks becomes a critical factor in DLP bioprinting since they would have to be maintained in the liquid state (e.g., room temperature) during the entire process to enable layer-by-layer biofabrication.[37, 40, 60] Therefore, the stability of our micropore-forming bioinks was evaluated using fluorescently labeled GelMA[28] (**Figure S15**). It could be found that an apparent phase-separation started to occur in the micropore-forming bioink made of HF-GelMA (10 wt.%) and PEO (1 wt.%, MW: 1×10^5 Da) after ca. 10 min of mixing at room temperature, consistent with our previous formulation reported.[28] Of note, in comparison, the emulsions formed with both PVA and dextran (2 wt.%, MW: 1×10^5 Da for both) as the dispersion phases exhibited excellent stabilities for as long as 120 min assessed, which is typically more than sufficient for a number of DLP bioprinting sessions. Thus, we selected dextran as the dispersion phase for the subsequent studies, also as a demonstration of the versatility of our toolbox in differentiation with PVA used above for extrusion bioprinting.

Similar to extrusion bioprinting, we evaluated the printability of our micropore-forming bioinks for DLP bioprinting, defined by successful lifting of a bioprinted layer without any noticeable damage in the layer integrity. Clearly, the bioinks with the continuous phases of LF-GelMA and MP-GelMA/HP-GelMA (10 wt.% for all) were difficult to bioprint due to the overly low rigidities post-photocrosslinking and the overly high viscosities prior to photocrosslinking, respectively (**Figure 6a**). In the case of lower HF-GelMA concentrations, it was similarly tricky

to bioprint a 3D hydrogel structure due to its fragility (**Figure 6b**). Furthermore, the higher dextran concentration or molecular weight resulting in larger micropore sizes, could induce either more significant light diffraction (**Figure S16**) causing weaker photocrosslinking or lead to mechanical instability due to the large micropore sizes themselves, both reducing printability (**Figure 6c**).

Once knowing the printability, we chose the micropore-forming bioink made of HF-GelMA (10 wt.%) and dextran (2 wt.%, MW: 5×10^5 Da) to showcase the DLP bioprinting capacities. By precisely designing the digital masks, various planar shapes with different levels of complexities, such as the 'BWH' badge, the Chinese character '福', and flowers and animals, were successfully produced (**Figure 6d**). Of note, for these 2D patterns the resolutions were found to be high. For example, while the pure HF-GelMA (10 wt.%) could be patterned at down to 96 ± 20 μm in line thickness, the micropore-forming HF-GelMA (10 wt.%) bioinks made with dextran at 1 wt.%, 2 wt.%, or 3 wt.% were similar in resolutions at 116 ± 20 μm, 136 ± 20 μm, or 152 ± 20 μm, respectively (**Figure 6e**). Moreover, the dextran concentration-induced emulsion droplet size-increase was well-preserved in the bioprinted patterns, reflected by the increase in the micropore sizes (**Figure 6f**).

Also critical, in our initial version of the micropore-forming bioink solely relying on a single type of GelMA (pork) and a single type of porogen (PEO) with a single molecular weight (3×10^5 Da),[28-30] the printability for DLP bioprinting in particular, was very poor; although this bioink formulation was patternable with DLP, only single-layer structures could be created as we previously illustrated.[28] Here with our micropore-forming GelMA bioink toolbox 2.0 that allows much better controllability of the bioink viscosities, mechanical properties, and other parameters, truly volumetric constructs of complex shapes containing sophisticated internal architectures, could be bioprinted, realizing the full potential of the DLP modality. As examples, we successfully achieved bioprinting of a solid, rounded trapezoid, a rectangular cube embedded with a single, hollow, perfusable microchannel, as well as a rectangular cube containing a perfusable hierarchical microchannel that had one inlet on the left and two outlets on the left (**Figure 6g**).

Finally, cellular behaviors in DLP-bioprinted microporous HF-GelMA hydrogel constructs were assessed. NIH/3T3 fibroblasts and HepG2 cells were encapsulated in bioprinted thick clover patterns. Consistent with extrusion bioprinting (**Figure S14**), both cell types displayed higher cell viability values over the 7 days of culture (**Figure S17**). Morphological observations further proved that the HepG2 cells proliferated over time within the bioprinted microporous HF-GelMA

hydrogels showing significant aggregate-formation (**Figure 6h**). Quantitative analyses of albumin and urea secretions further revealed functional improvements of HepG2 cells when embedded in our microporous HF-GelMA hydrogels compared to the control, non-microporous HF-GelMA hydrogels (**Figure S18**). Collectively, our results demonstrated the tunable properties of the micropore-forming GelMA bioinks, which when coupled with DLP bioprinting, could facilitate the generation of a multitude of cell-laden microporous hydrogel constructs featuring more sophisticated shapes and internal architectures, for tissue engineering and related applications.

4. Conclusions

In summary, we have developed a series of ATPE-enabled micropore-forming bioinks, which we term as the 'micropore-forming GelMA bioink toolbox 2.0', for efficient fabrication of cell-laden hydrogels with interconnected microporous structures. These bioinks feature widely adjustable micropore sizes, mechanical performances, rheological properties, and cellular activities by precisely tuning their compositions in terms of GelMA type, degree of methacryloyl-modification, as well as porogen type, molecular weight, and concentration. As such, our toolbox also allows broad adaptability for bioprinting using, as demonstrated, for example, extrusion and DLP modalities. We believe that with further development, our micropore-forming GelMA bioink toolbox 2.0 will provide a reliable resource for biomanufacturing of 2D and 3D cell-laden tissue constructs using not only bioprinting methods already demonstrated but also other modalities as well as other biofabrication techniques, which will find great use in areas such as tissue engineering, regenerative medicine, and pharmaceutical screening.

Supporting Information

Supporting Information is available from the Wiley Online Library or from the author.

Acknowledgements

This work was supported by the Brigham Research Institute.

References

[1] A. Atala, F. K. Kasper, A. G. Mikos, Sci. Transl. Med. 2012, 4, 160rv12.

[2] A. Khademhosseini, R. Langer, Nat. Protoc. 2016, 11, 1775.

[3] Y. S. Zhang, A. Khademhosseini, Science 2017, 356, eaaf3627.

[4] M. P. Lutolf, Nature Materials 2009, 8, 451.
[5] A. Al-Abboodi, J. Fu, P. M. Doran, T. T. Tan, P. P. Chan, Adv Healthc Mater 2014, 3, 725.
[6] R. Gauvin, Y. C. Chen, J. W. Lee, P. Soman, P. Zorlutuna, J. W. Nichol, H. Bae, S. Chen, A. Khademhosseini, Biomaterials 2012, 33, 3824.
[7] D. L. Elbert, Acta Biomater 2011, 7, 31.
[8] S. W. Choi, Y. Zhang, M. R. Macewan, Y. N. Xia, Adv. Healthcare Mater. 2013, 2, 145.
[9] A. Ovsianikov, A. Deiwick, S. Van Vlierberghe, P. Dubruel, L. Moller, G. Drager, B. Chichkov, Biomacromolecules 2011, 12, 851.
[10] S. H. Oh, I. K. Park, J. M. Kim, J. H. Lee, Biomaterials 2007, 28, 1664.
[11] D. J. Griffon, M. R. Sedighi, D. V. Schaeffer, J. A. Eurell, A. L. Johnson, Acta Biomaterialia 2006, 2, 313.
[12] K. Whang, K. E. Healy, D. R. Elenz, E. K. Nam, D. C. Tsai, C. H. Thomas, G. W. Nuber, F. H. Glorieux, R. Travers, S. M. Sprague, Tissue Engineering 1999, 5, 35.
[13] L. Moroni, J. A. Burdick, C. Highley, S. J. Lee, Y. Morimoto, S. Takeuchi, J. J. Yoo, Nature Reviews Materials 2018, 3, 21.
[14] S. V. Murphy, P. De Coppi, A. Atala, Nature biomedical engineering 2019, 1.
[15] P. D. Dalton, T. B. F. Woodfield, V. Mironov, J. Groll, Advanced Science 2020, 7, 1902953.
[16] R. Levato, T. Jungst, R. G. Scheuring, T. Blunk, J. Groll, J. Malda, Adv. Mater. 2020, 32, 1906423.
[17] M. Costantini, J. Jaroszewicz, L. Kozon, K. Szlazak, W. Swieszkowski, P. Garstecki, C. Stubenrauch, A. Barbetta, J. Guzowski, Angew Chem Int Ed Engl 2019, 58, 7620.
[18] R. Hatti-Kaul, Molecular Biotechnology 2001, 19, 269.
[19] Y. Chao, H. C. Shum, Chem. Soc. Rev. 2020, 49, 114.
[20] H. Tavana, A. Jovic, B. Mosadegh, Q. Y. Lee, X. Liu, K. E. Luker, G. D. Luker, S. J. Weiss, S. Takayama, Nat Mater 2009, 8, 736.
[21] Y. Chao, S. Y. Mak, S. Rahman, S. Zhu, H. C. Shum, Small 2018, 14, e1802107.
[22] A. Madadlou, A. Saint-Jalmes, F. Guyomarc'h, J. Floury, D. Dupont, Food Hydrocolloids 2019, 93, 351.
[23] J. M. Lee, E.-S. Chan, R. Nagasundara Ramanan, C. W. Ooi, Fluid Phase Equilibria 2020, 508.
[24] Y. Chao, S. Y. Mak, S. Rahman, S. Zhu, H. C. Shum, Small 2018, 14, 1802107.
[25] Y. Wang, R. K. Kankala, J. Zhang, L. Hao, K. Zhu, S. Wang, Y. S. Zhang, A. Chen, Advanced Science 2020, 7, 2002002.
[26] A. G. Teixeira, R. Agarwal, K. R. Ko, J. Grant-Burt, B. M. Leung, J. P. Frampton, Advanced Healthcare Materials 2018, 7.
[27] H. Yuan, Q. Ma, Y. Song, M. Y. H. Tang, Y. K. Chan, H. C. Shum, Macromolecular Chemistry and Physics 2017, 218.
[28] G.-L. Ying, N. Jiang, S. Maharjan, Y.-X. Yin, R.-R. Chai, X. Cao, J.-Z. Yang, A. K. Miri, S. Hassan, Y. S. Zhang, Adv. Mater. 2018, 30, 1805460.
[29] G. Ying, N. Jiang, C. Parra-Cantu, G. Tang, J. Zhang, H. Wang, S. Chen, N.-P. Huang, J. Xie, Y. S. Zhang, Adv. Funct. Mater. 2020, 30, 2003740.
[30] G. Ying, J. Manríquez, D. Wu, J. Zhang, N. Jiang, S. Maharjan, D. H. Hernández Medina, Y. S. Zhang, Materials Today Bio 2020, 8, 100074.
[31] K. Yue, X. Li, K. Schrobback, A. Sheikhi, N. Annabi, J. Leijten, W. Zhang, Y. S. Zhang, D. W. Hutmacher, T. J. Klein, Biomaterials 2017, 139, 163.

[32] J. Gong, C. Shuurmans, X. Cao, A. M. Van Genderen, W. Li, F. Cheng, J. J. He, A. López, V. Huerta, J. Manríquez, R. Li, H. Li, C. Delavaux, S. Sebastian, H. Wang, J. Xie, M. Yu, R. Masereeuw, T. Vermonden, Y. S. Zhang, Nature Communications 2020, 11, 1267.

[33] S. Maharjan, J. Alva, C. Cámara, A. G. Rubio, D. Hernández, C. Delavaux, E. Correa, M. D. Romo, D. Bonilla, M. L. Santiago, W. Li, F. Cheng, G. Ying, Y. S. Zhang, Matter 2021, 4, 217.

[34] W. Liu, M. A. Heinrich, Y. Zhou, A. Akpek, N. Hu, X. Liu, X. Guan, Z. Zhong, X. Jin, A. Khademhosseini, Y. S. Zhang, Adv. Healthcare Mater. 2017, 6, 1601451.

[35] A. K. Miri, D. Nieto, L. Iglesias, H. Goodarzi Hosseinabadi, S. Maharjan, G. U. Ruiz-Esparza, P. Khoshakhlagh, A. Manbachi, M. R. Dokmeci, S. Chen, S. R. Shin, Y. S. Zhang, A. Khademhosseini, Adv. Mater. 2018, 30, 1800242.

[36] W. Li, M. Wang, L. S. Mille, J. A. Robledo, V. Huerta, T. Uribe, F. Cheng, H. Li, J. Gong, T. Ching, C. A. Murphy, A. Lesha, S. Hassan, T. B. F. Woodfield, K. S. Lim, Y. S. Zhang, Adv. Mater. 2021, 33, 2102153.

[37] M. Wang, W. Li, L. S. Mille, T. Ching, Z. Luo, G. Tang, C. E. Garciamendez, A. Lesha, M. Hashimoto, Y. S. Zhang, Adv. Mater. 2021, n/a, 2107038.

[38] K. S. Lim, B. S. Schon, N. V. Mekhileri, G. C. J. Brown, C. M. Chia, S. Prabakar, G. J. Hooper, T. B. F. Woodfield, ACS Biomaterials Science & Engineering 2016, 2, 1752.

[39] H. J. Yoon, S. R. Shin, J. M. Cha, S.-H. Lee, J.-H. Kim, J. T. Do, H. Song, H. Bae, PLoS One 2016, 11, e0163902.

[40] R. Levato, K. S. Lim, W. Li, A. U. Asua, L. B. Peña, M. Wang, M. Falandt, P. N. Bernal, D. Gawlitta, Y. S. Zhang, T. B. F. Woodfield, J. Malda, Materials Today Bio 2021, 12, 100162.

[41] A. Gustafsson, H. Wennerstrom, F. Tjerneld, Polymer 1986, 27, 1768.

[42] K. Wysoczanska, E. A. Macedo, Journal of Chemical & Engineering Data 2016, 61, 4229.

[43] A. G. Teixeira, R. Agarwal, K. R. Ko, J. Grant-Burt, B. M. Leung, J. P. Frampton, Adv Healthc Mater 2018, 7, e1701036.

[44] J. Esquena, Current Opinion in Colloid & Interface Science 2016, 25, 109.

[45] N. A. Peppas, J. Z. Hilt, A. Khademhosseini, R. Langer, Advanced Materials 2006, 18, 1345.

[46] X. Zhao, Q. Lang, L. Yildirimer, Z. Y. Lin, W. Cui, N. Annabi, K. W. Ng, M. R. Dokmeci, A. M. Ghaemmaghami, A. Khademhosseini, Adv Healthc Mater 2016, 5, 108.

[47] M. A. Daniele, A. A. Adams, J. Naciri, S. H. North, F. S. Ligler, Biomaterials 2014, 35, 1845.

[48] G. Ying, N. Jiang, C. Yu, Y. S. Zhang, Bio-Design and Manufacturing 2018, 1, 215.

[49] C. M. Murphy, M. G. Haugh, F. J. O'brien, Biomaterials 2010, 31, 461.

[50] S. H. Oh, T. H. Kim, G. I. Im, J. H. Lee, Biomacromolecules 2010, 11, 1948.

[51] F. Bai, J. Zhang, Z. Wang, J. Lu, J. Chang, J. Liu, G. Meng, X. Dong, Biomed. Mater. 2011, 6, 015007.

[52] M. A. Heinrich, W. Liu, A. Jimenez, J. Yang, A. Akpek, X. Liu, Q. Pi, X. Mu, N. Hu, R. M. Schiffelers, J. Prakash, J. Xie, Y. S. Zhang, Small 2019, 15, 1805510.

[53] Y. Yu, K. K. Moncal, J. Li, W. Peng, I. Rivero, J. A. Martin, I. T. Ozbolat, Sci. Rep. 2016, 6, 1.

[54] O. Jeon, Y. B. Lee, H. Jeong, S. J. Lee, D. Wells, E. Alsberg, Materials Horizons 2019, 6, 1625.

[55] B. G. Soliman, G. C. J. Lindberg, T. Jungst, G. J. Hooper, J. Groll, T. B. F. Woodfield, K. S. Lim, Adv. Healthcare Mater. 2020, 9, 1901544.

[56] J. Yin, M. Yan, Y. Wang, J. Fu, H. Suo, ACS Appl Mater Interfaces 2018, 10, 6849.

[57] C. Yu, J. Schimelman, P. Wang, K. L. Miller, X. Ma, S. You, J. Guan, B. Sun, W. Zhu, S. Chen, Chem. Rev.

2020, 120, 10695.
[58] K. S. Lim, J. H. Galarraga, X. Cui, G. C. J. Lindberg, J. A. Burdick, T. B. F. Woodfield, Chem. Rev. 2020, 120, 10662.
[59] M. Lee, R. Rizzo, F. Surman, M. Zenobi-Wong, Chem. Rev. 2020, 120, 10950.
[60] W. Li, L. S. Mille, J. A. Robledo, T. Uribe, V. Huerta, Y. S. Zhang, Adv. Healthcare Mater. 2020, 9, 2000156.

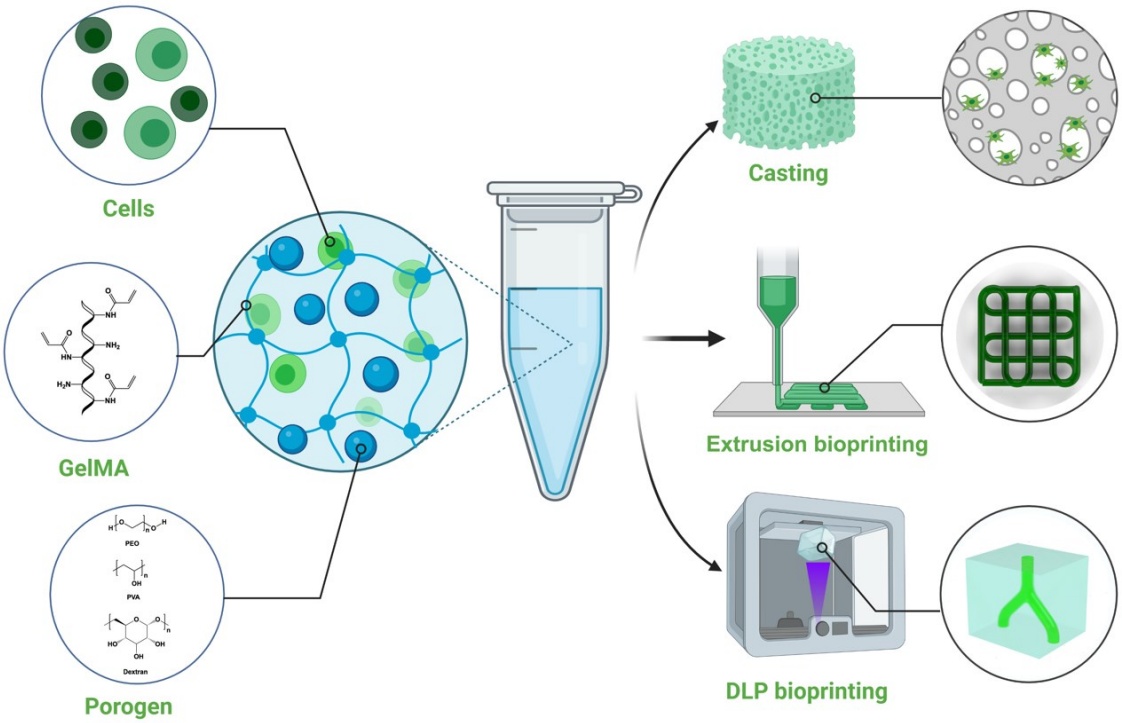

Figure 1. Schematics showing the design of our micropore-forming GelMA bioink toolbox 2.0 for applications towards 3D bioprinting.

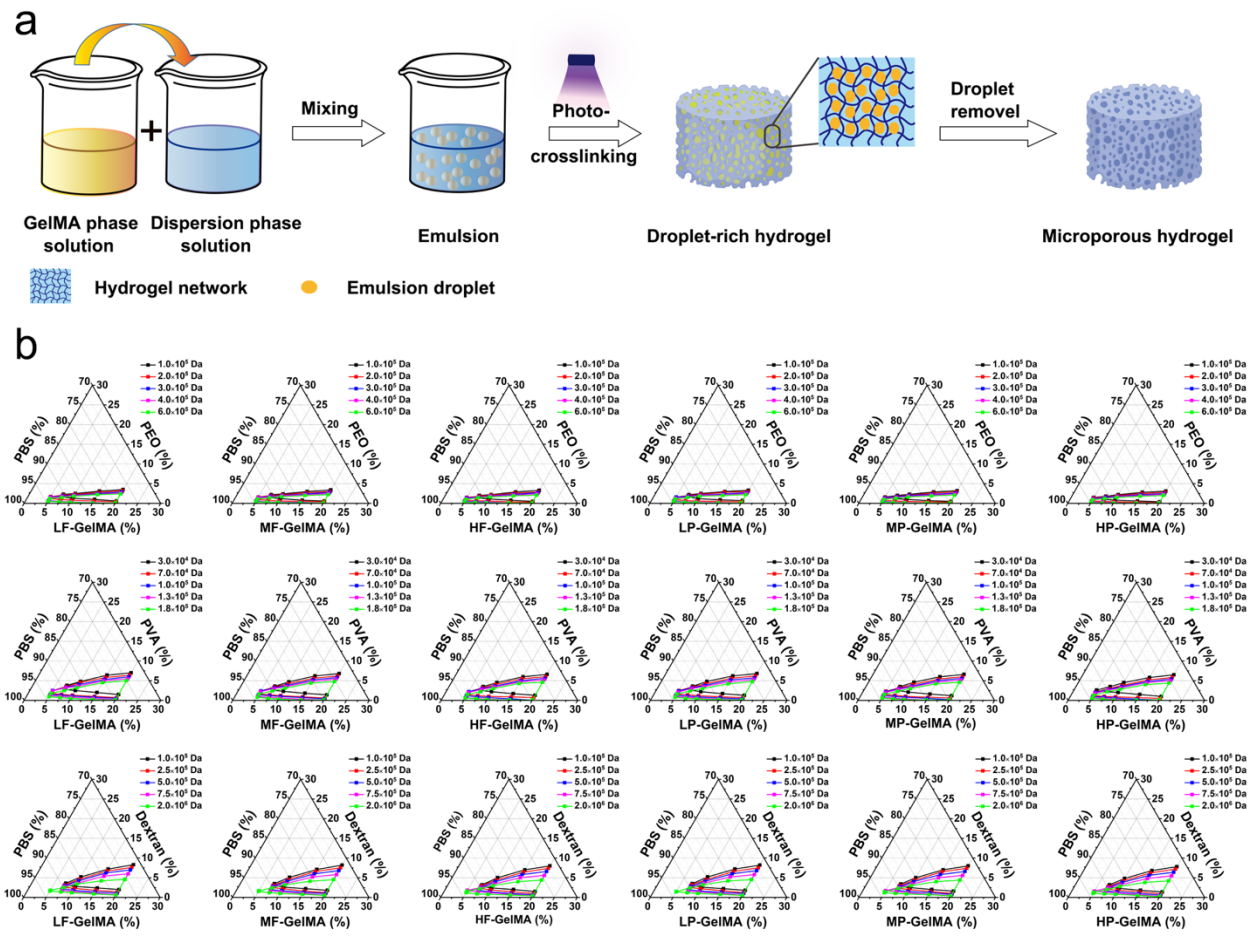

Figure 2. a) Schematics illustrating the preparation of the microporous GelMA hydrogel construct based on the APTE system-enabled micropore-forming bioink. b) Phase diagrams of the APTE-formation in our micropore-forming GelMA bioink toolbox 2.0, using PEO, PVA, and dextran with different molecular weights as the porogens, respectively.

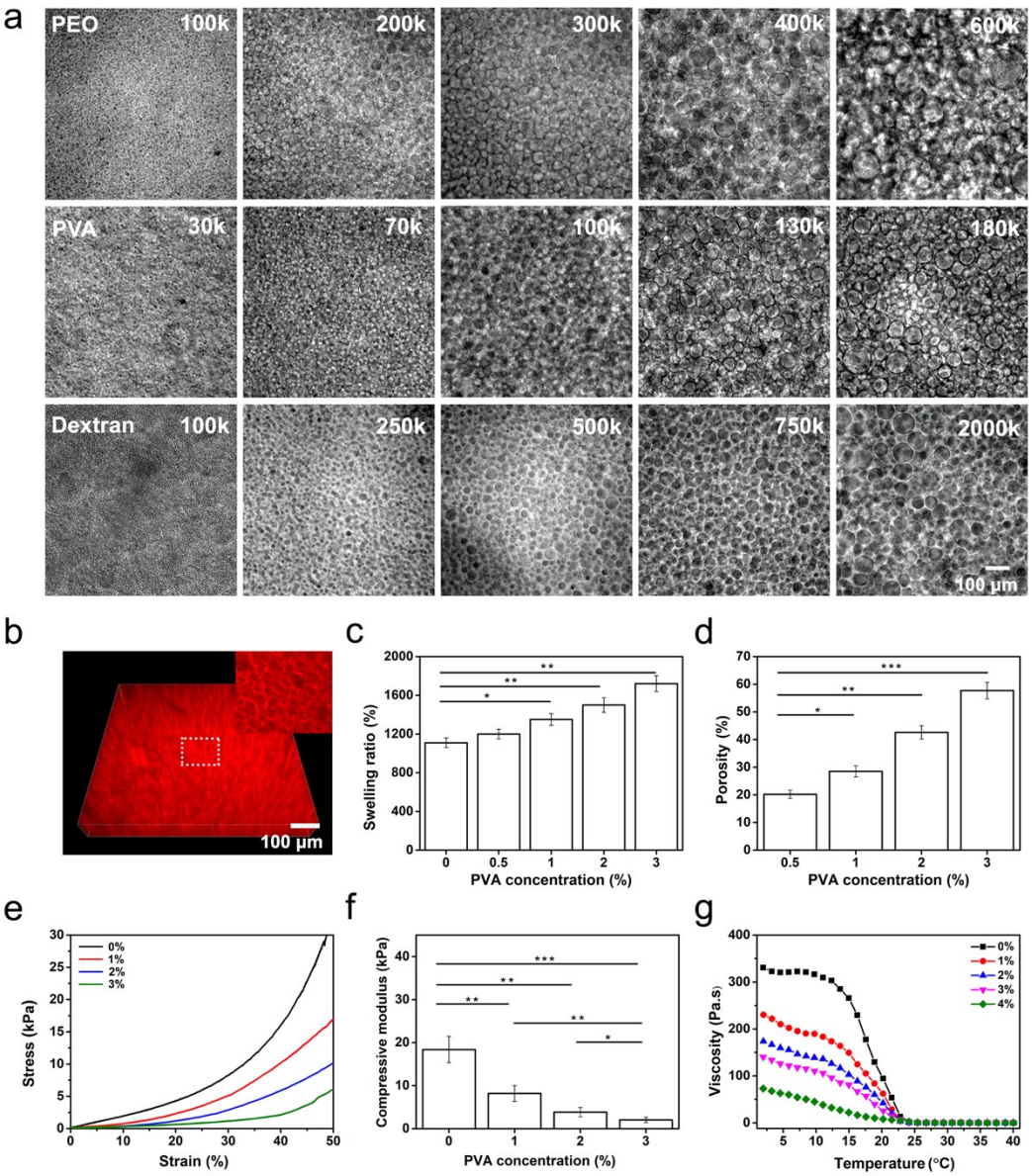

Figure 3. a) Microscopic images of the microporous MP-GelMA (10 wt.%) hydrogel constructs made with different porogens of PEO (1 wt.%), PVA (2 wt.%), and dextran (2 wt.%), taken immediately after hydrogel-formation. The number at top right corner of each image refers to the MW of the porogen. b) Confocal reconstruction fluorescence image of a microporous MP-GelMA hydrogel with interconnected pores; inset shows the top view. c) Swelling ratios, d) microscale porosities, e) compressive stress-strain curves, and f) compressive moduli of the microporous MP-GelMA (10 wt.%) hydrogels made with PVA as the porogen at different concentrations. g) Viscosities of the micropore-forming MP-GelMA (10 wt.%) bioinks made with PVA as the porogen at different concentrations, as a function of temperature, measured at the shear rate of 10

s^{-1}. In (d-h) the molecular weight of PVA was 1×10^5 Da. (*p<0.05, **p<0.01, and ***p<0.001, n=3)

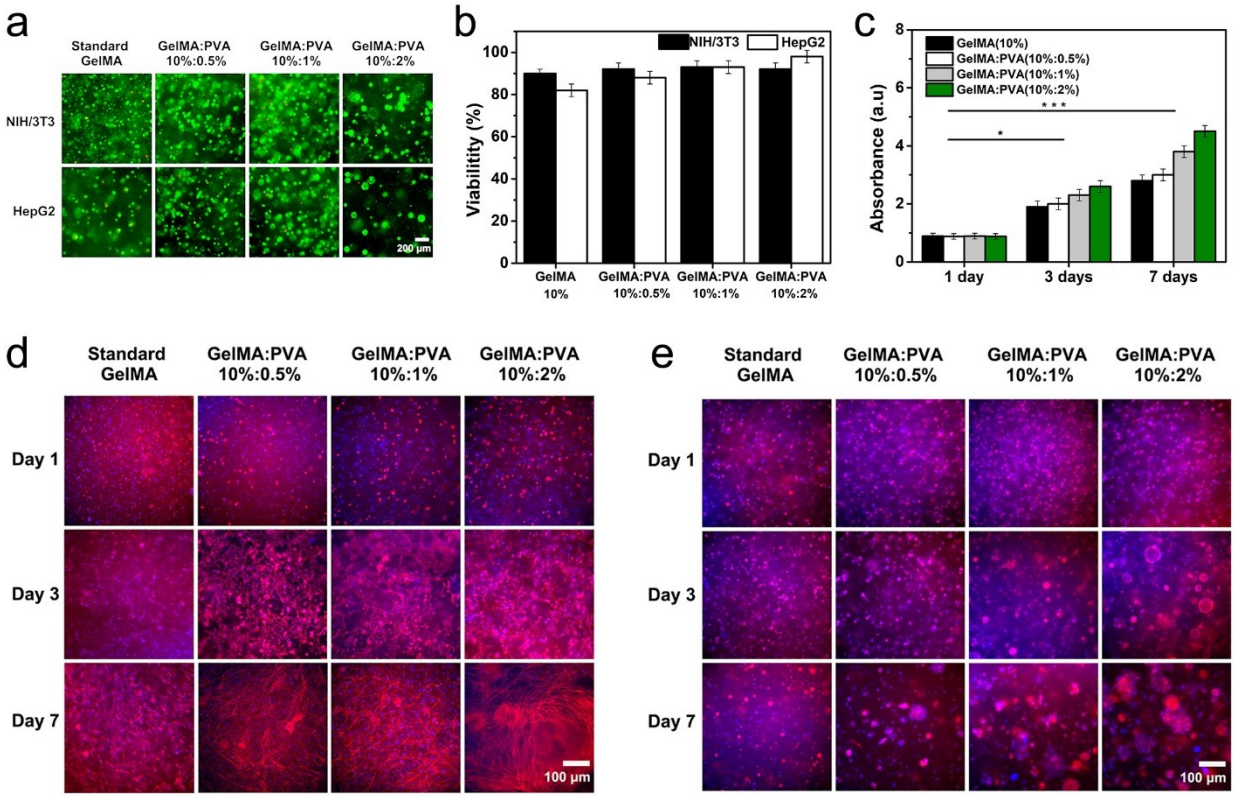

Figure 4. a) Fluorescence micrographs showing viabilities of encapsulated NIH/3T3 fibroblasts and HepG2 cells in HF-GelMA hydrogels without or with different micropore sizes on Day 7 of culture, where live cells were stained in green and dead cells in red. b) Quantification analyses of the cell viabilities in HF-GelMA hydrogels without or with different micropore sizes on Day 7 of culture. c) Quantification analyses of proliferation of HepG2 cells on 1, 3, and 7 days of culture in HF-GelMA hydrogels without or with different micropore sizes. d, e) Fluorescence micrographs of (d) NIH/3T3 fibroblasts and (e) HepG2 cells showing cell spreading or aggregation in HF-GelMA hydrogels without or with different micropore sizes on 1, 3, and 7 days of culture. The cells were stained for F-actin (red) and nuclei (blue). In (a-e) the molecular weight of PVA was 1×10^5 Da. (*$p<0.05$, **$p<0.01$, and ***$p<0.001$, n=3)

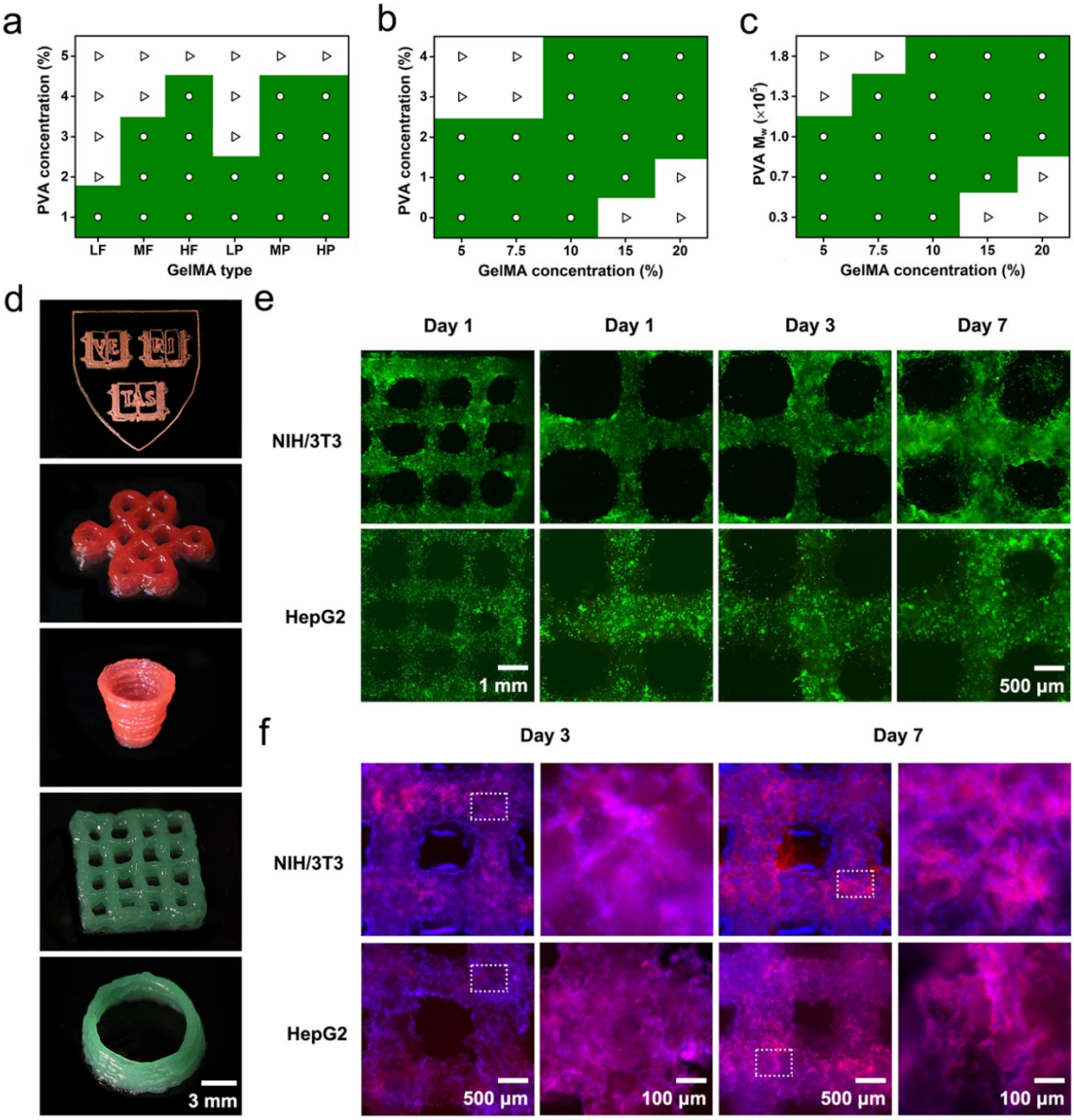

Figure 5. a-c) Printability maps of the GelMA/PVA micropore-forming bioinks for extrusion bioprinting. In (a, b) the molecular weight of PVA was 1×10^5 Da. In (c) the concentration of PVA was 1%. d) Photographs showing extrusion-bioprinted single-layered and multilayered microporous GelMA patterns. e) Fluorescence micrographs showing viability of encapsulated NIH/3T3 fibroblasts and HepG2 cells in bioprinted microporous GelMA patterns on 1, 3, and 7 days of culture, where live cells were stained in green and dead cells in red. f) Fluorescence micrographs showing morphologies of NIH/3T3 fibroblasts and HepG2 cells in bioprinted microporous GelMA patterns on 3 and 7 days of culture, where the cells were stained for F-actin (red) and nuclei (blue). In (d-f) the bioink was made of HF-GelMA (10 wt.%) and PVA (1 wt.%,

MW: 1×10^5 Da).

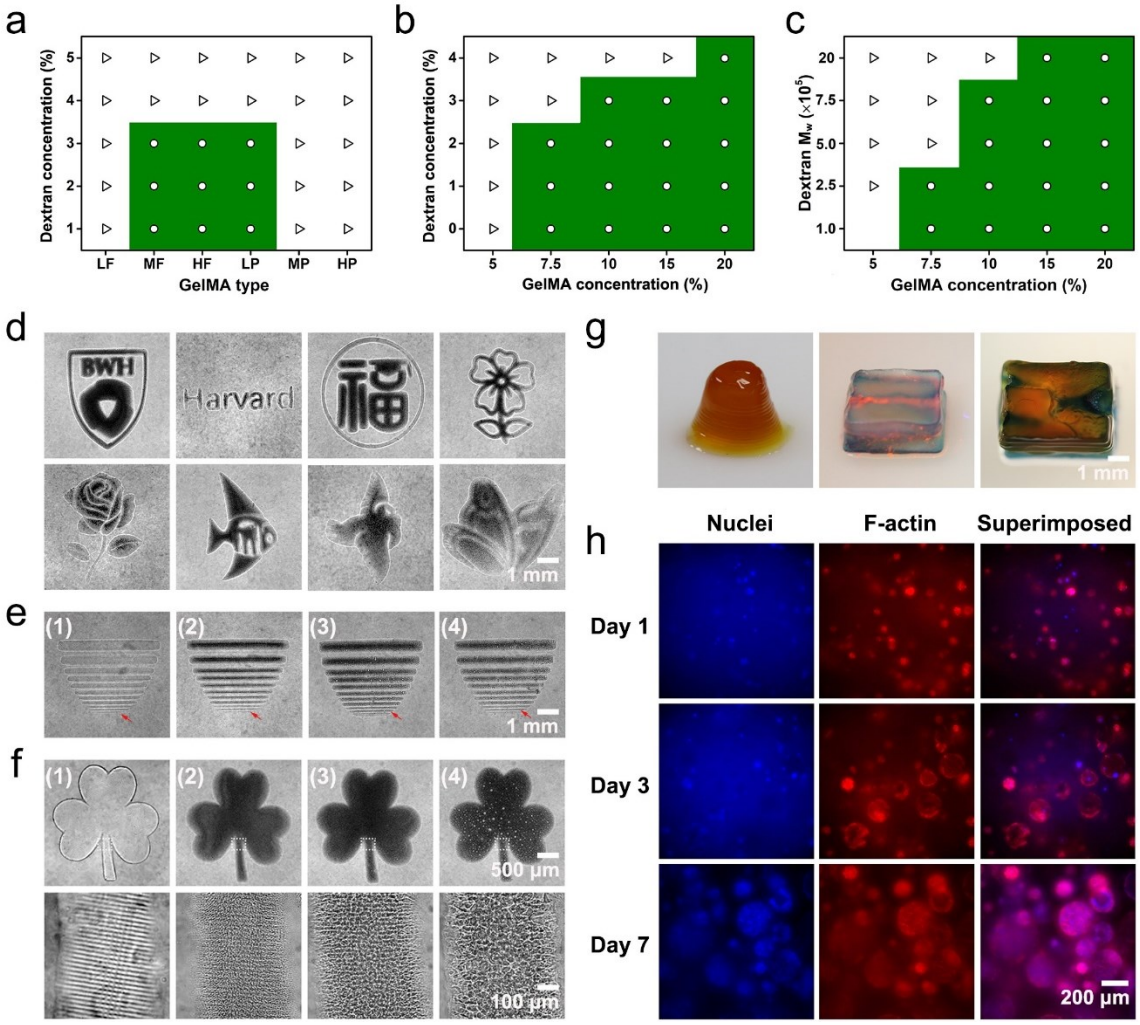

Figure 6. a-c) Printability maps of the GelMA/dextran micropore-forming bioinks for DLP bioprinting. In (a, b) the MW of dextran was 5×10^5 Da. In (c) the concentration of dextran was 2 wt.%. d) Micrographs showing DLP-bioprinted planar microporous GelMA patterns. The bioink was made of HF-GelMA (10 wt.%) and dextran (2 wt.%, MW: 5×10^5 Da). e) Micrographs showing the resolutions of DLP bioprinting using (1) standard GelMA bioink and (2-4) micropore-forming GelMA bioinks. f) Micrographs showing DLP-bioprinted clover patterns using (1) standard GelMA bioink and (2-4) micropore-forming GelMA bioinks. In (e-f, 2-4) the bioinks were made of HF-GelMA (10 wt.%) and 1, 2, and 3 wt.% dextran (MW: 5×10^5 Da), respectively. g) Photographs showing DLP-bioprinted 3D microporous GelMA hydrogel constructs featuring various shapes and internal structures. h) Fluorescence micrographs showing morphologies of HepG2 cells in DLP-bioprinted microporous GelMA constructs on Day 7 of culture, where the cells were stained for F-actin (red) and nuclei (blue). In (g, h) the bioink was made of HF-GelMA

(10 wt.%) and dextran (2 wt.%, MW: 5×10^5 Da).

Supplementary information

Micropore-Forming Gelatin Methacryloyl (GelMA) Bioink Toolbox 2.0: Designable Tunability and Adaptability for 3D Bioprinting Applications

Sili Yi, Qiong Liu, Zeyu Luo, Jacqueline Jialu He, Hui-Lin Ma, Wanlu Li, Di Wang, Cuiping Zhou, Carlos Ezio Garciamendez, Linxi Hou, Jin Zhang, Yu Shrike Zhang*

Dr. S. Yi, Dr. Q. Liu, Z Luo, J. J. He, H.-L. Ma, W. Li, D. Wang, Dr. C. Zhou, C. E. Garciamendez, Prof. Y. S. Zhang
Division of Engineering in Medicine
Department of Medicine
Brigham and Women's Hospital
Harvard Medical School
Cambridge, MA 02139, USA
E-mail: yszhang@research.bwh.harvard.edu

Dr. S. Yi, Prof. L. Hou, Prof. J. Zhang
College of Chemical Engineering
Fuzhou University
Fuzhou 350108, P.R. China

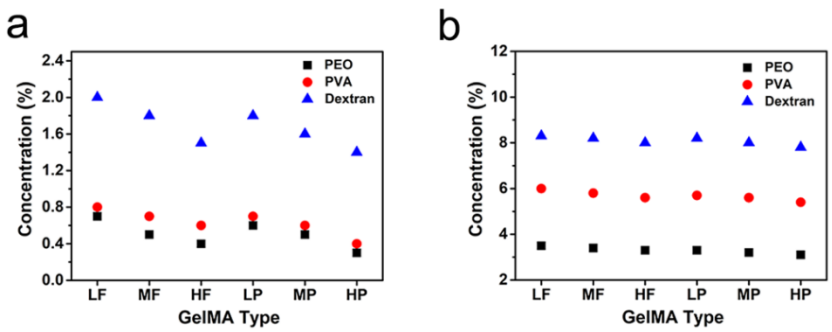

Figure S1. Critical concentrations of the porogens (MW for all: 1×10^5 Da) in formations of the APTEs with a) porcine and b) fish GelMA (10 wt.%).

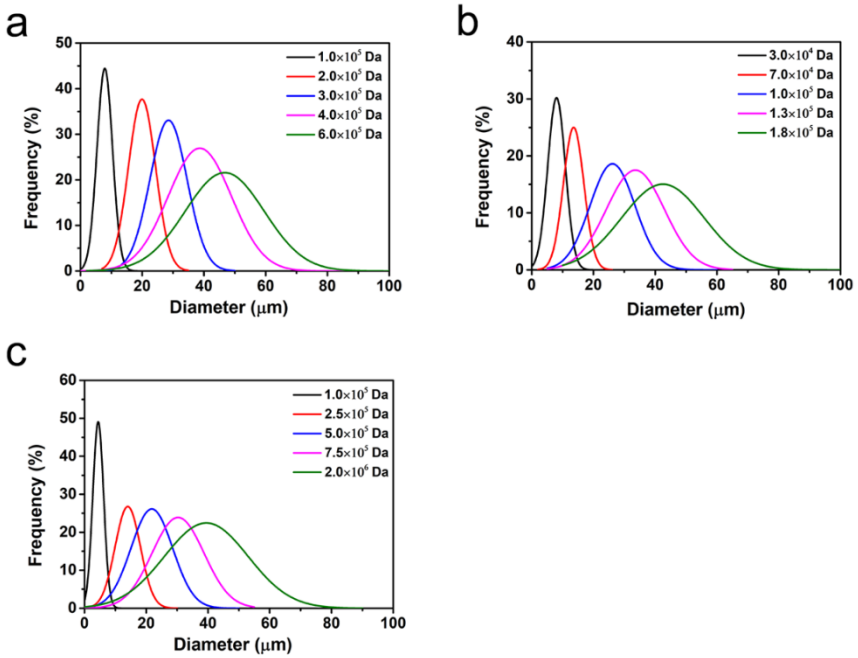

Figure S2. Micropore size distributions in the resulting MP-GelMA (10 wt.%) hydrogels made with a) PEO (1 wt.%), b) PVA (2 wt.%), and c) dextran (2 wt.%) as the porogens.

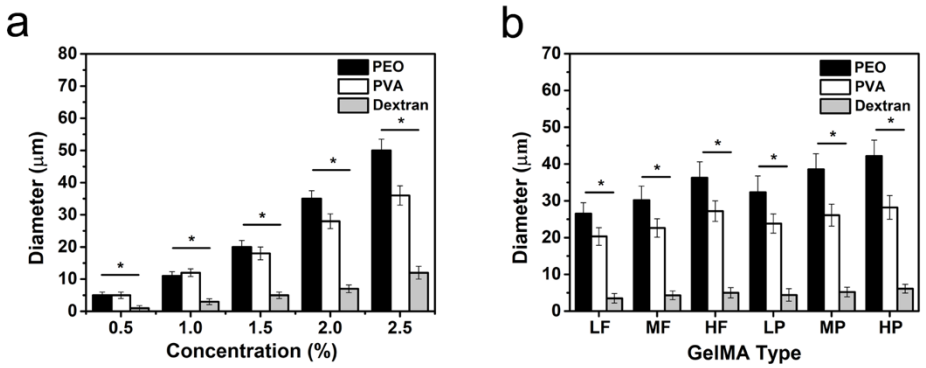

Figure S3. a) Effects of the type and concentration of porogen (MW for all: 1×10^5 Da) on micropore size of the resulting MP-GelMA (10 wt.%) hydrogels. b) Effect of the type of GelMA (10 wt.% in all cases) on micropore size of the resulting hydrogels, where the porogens were all 2 wt.% with molecular weight of 1×10^5 Da. (*$p<0.05$, n=3)

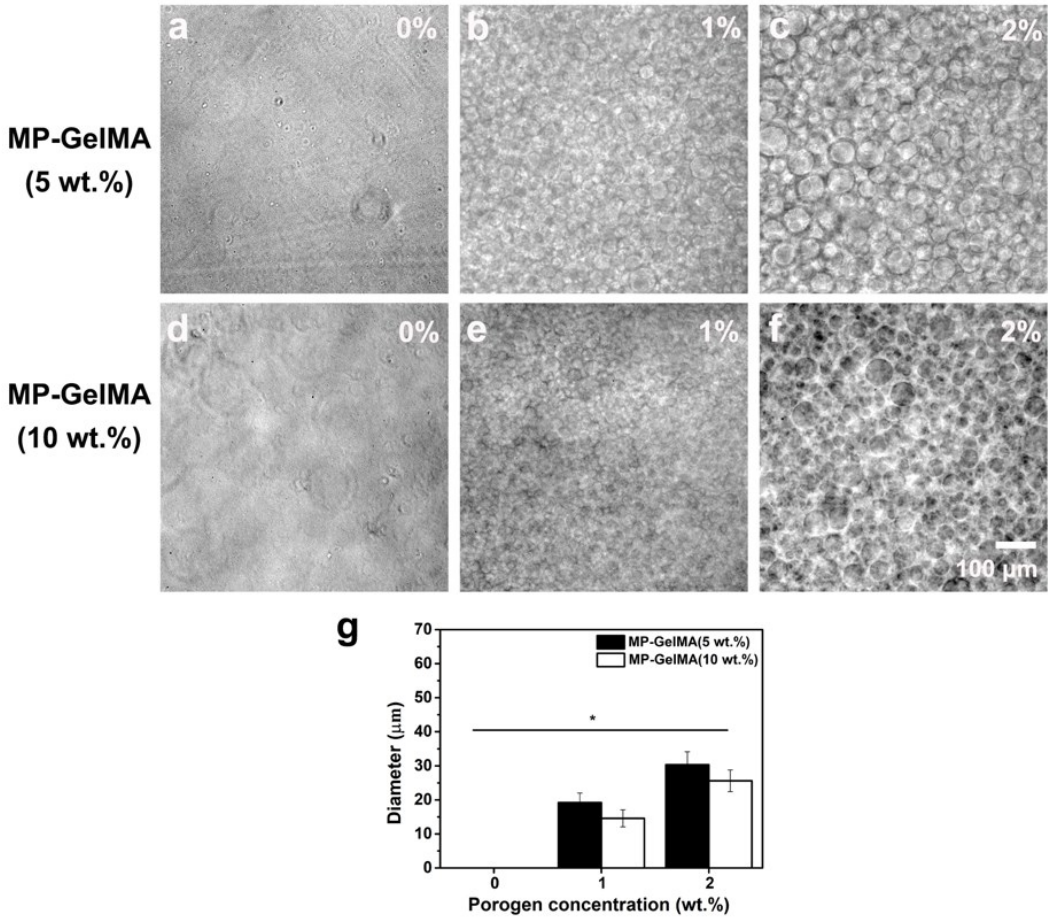

Figure S4. (a-f) Effect of concentration of dextran (MW: 1×10^5 Da) on micropore size of the resulting MP-GelMA (5 wt.% and 10 wt.%) hydrogels. (g) Quantification data.

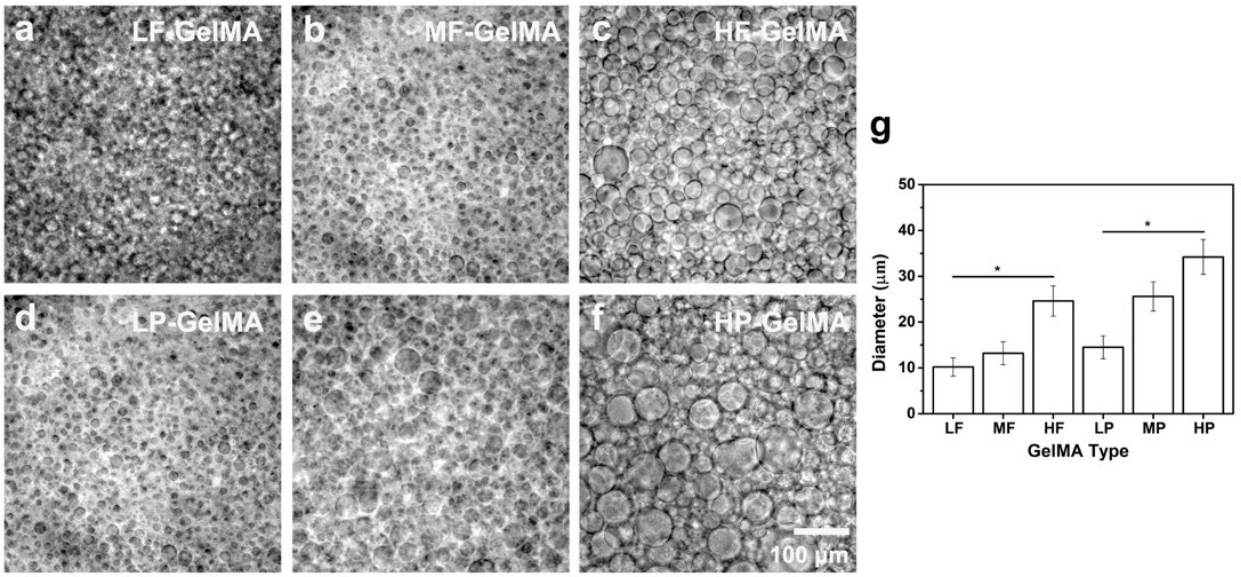

Figure S5. (a-f) Effect of GelMA type (10 wt.% in all cases) on micropore size of the resulting hydrogels, where dextran (2 wt.%, MW: 5×10^5 Da) was used as the porogen in all cases. (g) Quantification data.

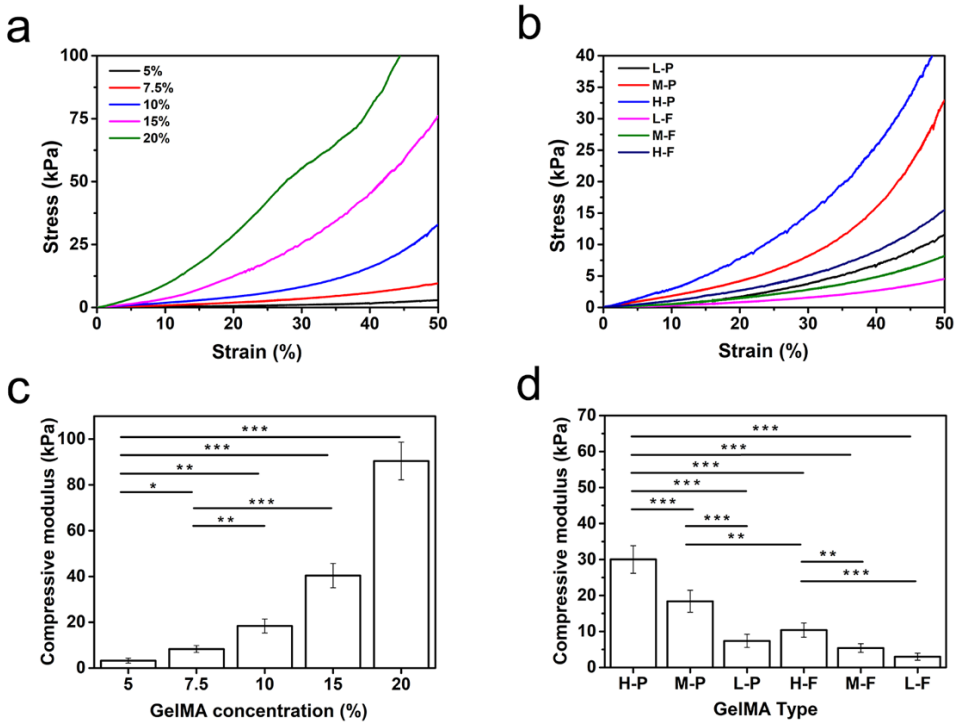

Figure S6. a) Compressive stress-strain curves of the microporous MP-GelMA hydrogels as a function of GelMA concentration. b) Compressive stress-strain curves of the microporous GelMA (10 wt.%) hydrogels as a function of GelMA type. c) Compressive moduli of the microporous MP-GelMA hydrogels as a function of GelMA concentration. d) Compressive moduli of the microporous GelMA (10 wt.%) hydrogels as a function of GelMA type. PVA (1 wt.%, MW: 1×10^5 Da) was used as the porogen in all cases. (*$p<0.05$, **$p<0.01$, and ***$p<0.001$, n=3)

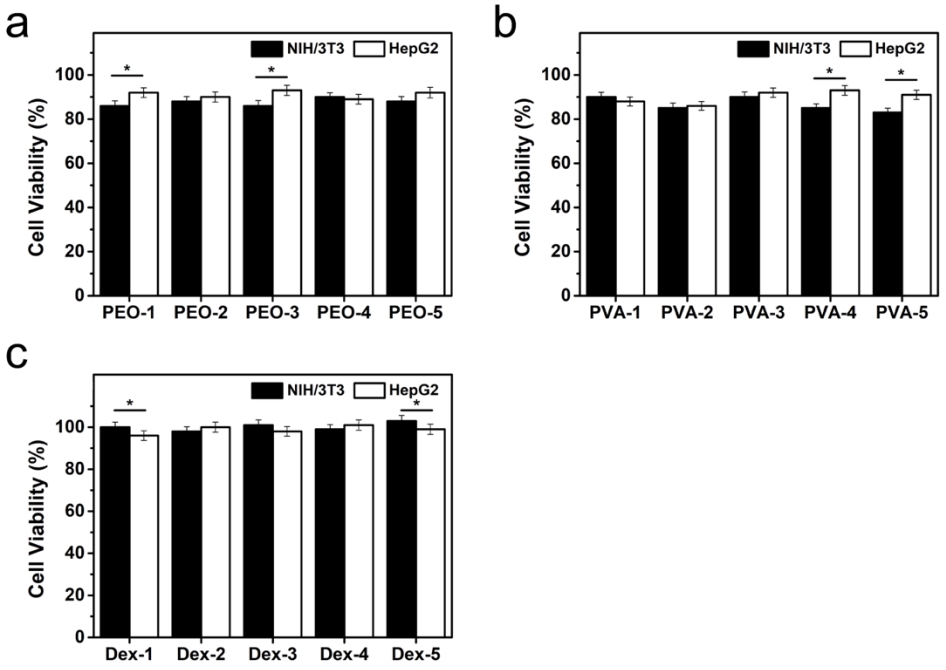

Figure S7. Cell viability values in culture media containing different porogen types all at 4 wt.% for a) PEO, where PEO-1, PEO-2, PEO-3, PEO-4, and PEO-5 denote PEO with MW of 1×10^5 Da, 2×10^5 Da, 3×10^5 Da, 4×10^5 Da, and 6×10^5 Da, respectively; b) PVA, where PVA-1, PVA-2, PVA-3, PVA-4, and PVA-5 denote PVA with MW of 3×10^4 Da, 7×10^4 Da, 1×10^5 Da, 1.3×10^5 Da, and 1.8×10^5 Da, respectively; and c) dextran, where Dex-1, Dex-2, Dex-3, Dex-4, and Dex-5 denote dextran with MW of 1×10^5 Da, 2.5×10^5 Da, 5×10^5 Da, 7.5×10^5 Da, and 2×10^6 Da, respectively. (*$p<0.05$, n=3)

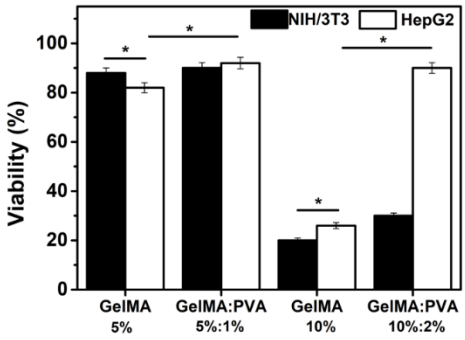

Figure S8. Cell viability in different MP-GelMA hydrogels after 7 days of cultivation. Molecular weight of PVA: 1×10^5 Da. (*$p<0.05$, $n=3$)

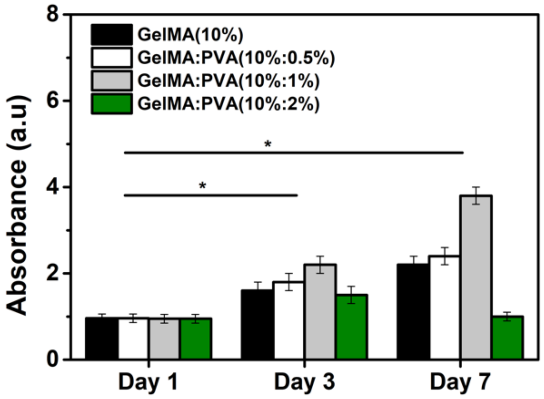

Figure S9. Quantification of proliferation of NIH/3T3 fibroblasts on Day 1, Day 3, and Day 7 in different HF-GelMA hydrogels using the PrestoBlue® assay. MW of PVA: 1×10^5 Da. (*$p<0.05$, n=3)

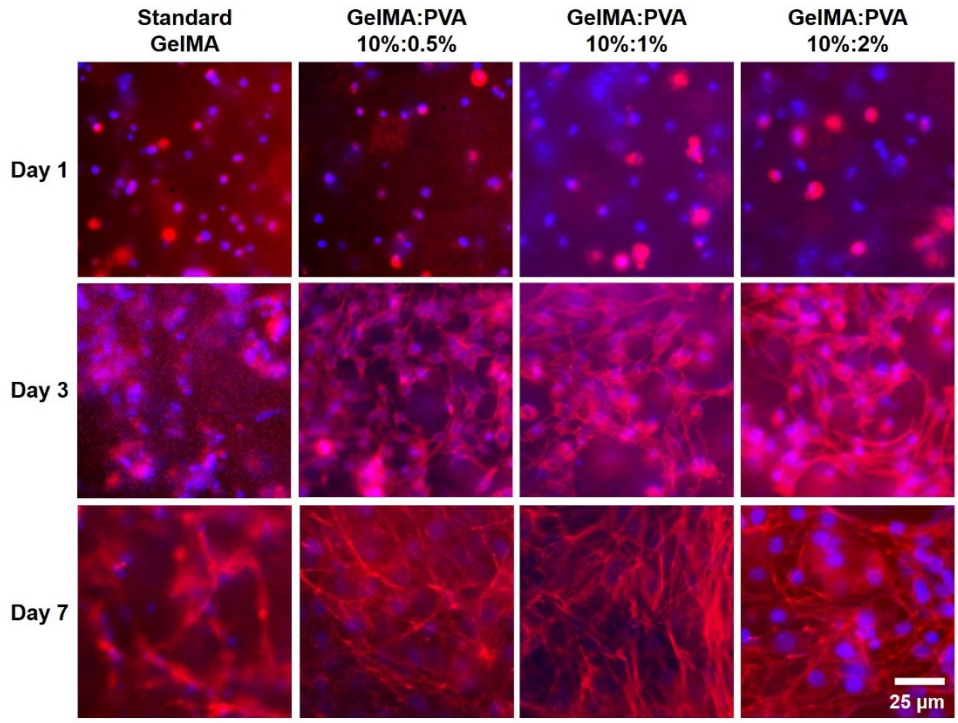

Figure S10. Fluorescence micrographs of NIH/3T3 fibroblasts showing cell spreading in HF-GelMA hydrogels without or with different micropore sizes on 1, 3, and 7 days of culture, corresponding to the images shown in **Figure 4d**. The cells were stained for F-actin (red) and nuclei (blue).

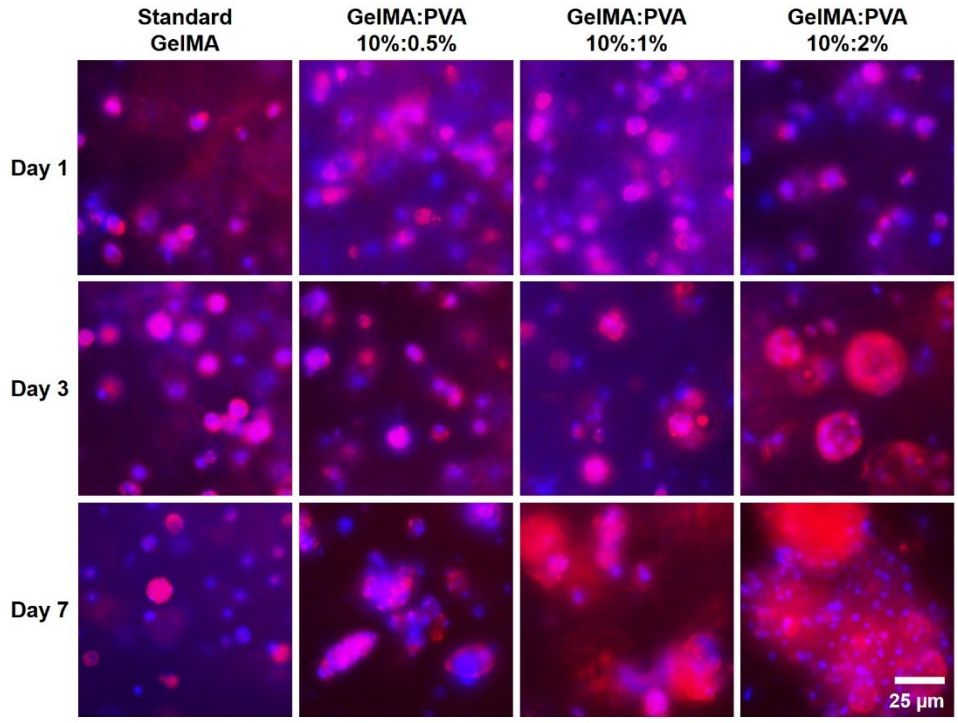

Figure S11. Fluorescence micrographs of HepG2 cells showing cell aggregation in HF-GelMA hydrogels without or with different micropore sizes on 1, 3, and 7 days of culture, corresponding to the images shown in **Figure 4e**. The cells were stained for F-actin (red) and nuclei (blue).

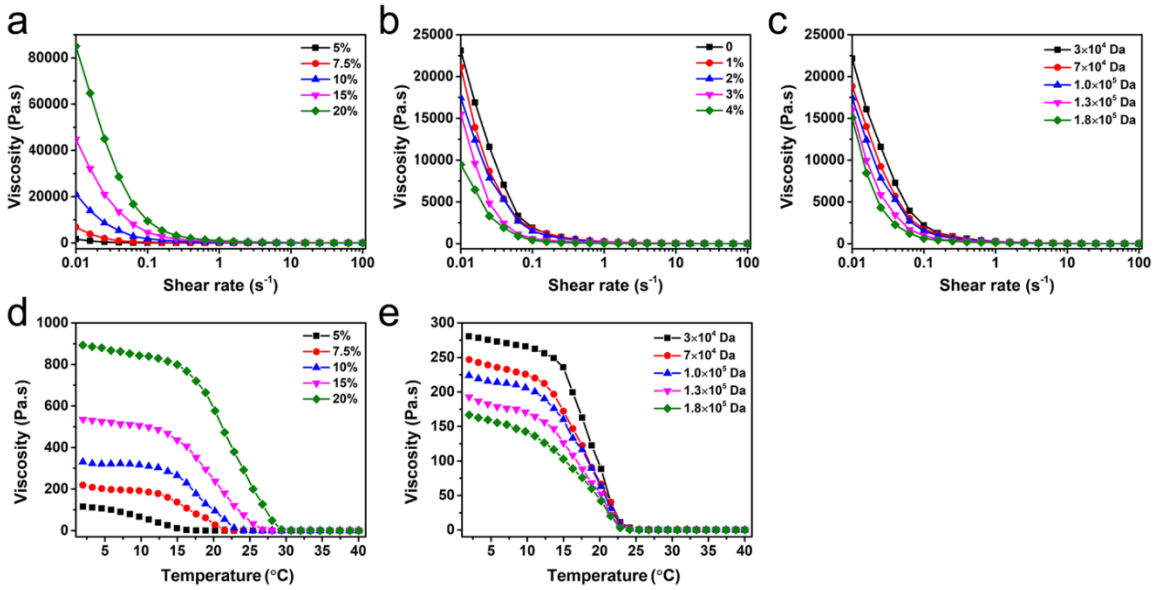

Figure S12. a) Viscosity values of pure MP-GelMA bioinks of different concentrations as a function of shear rate, measured at 25 °C. b) Viscosity values of MP-GelMA (10 wt.%) bioinks with different concentrations of PVA (MW: 1×10^5 Da) as a function of shear rate, measured at 25 °C. (c) Viscosity values of MP-GelMA bioinks with different molecular weights of PVA (2 wt.%) as a function of shear rate, measured at 25 °C. (d) Viscosity values of MP-GelMA bioinks of different concentrations as a function of temperature, measured at the shear rate of 10 s^{-1}. (e) Viscosity values of MP-GelMA (10 wt.%) bioinks with different molecular weights of PVA (2 wt.%) as a function of temperature, measured at the shear rate of 10 s^{-1}.

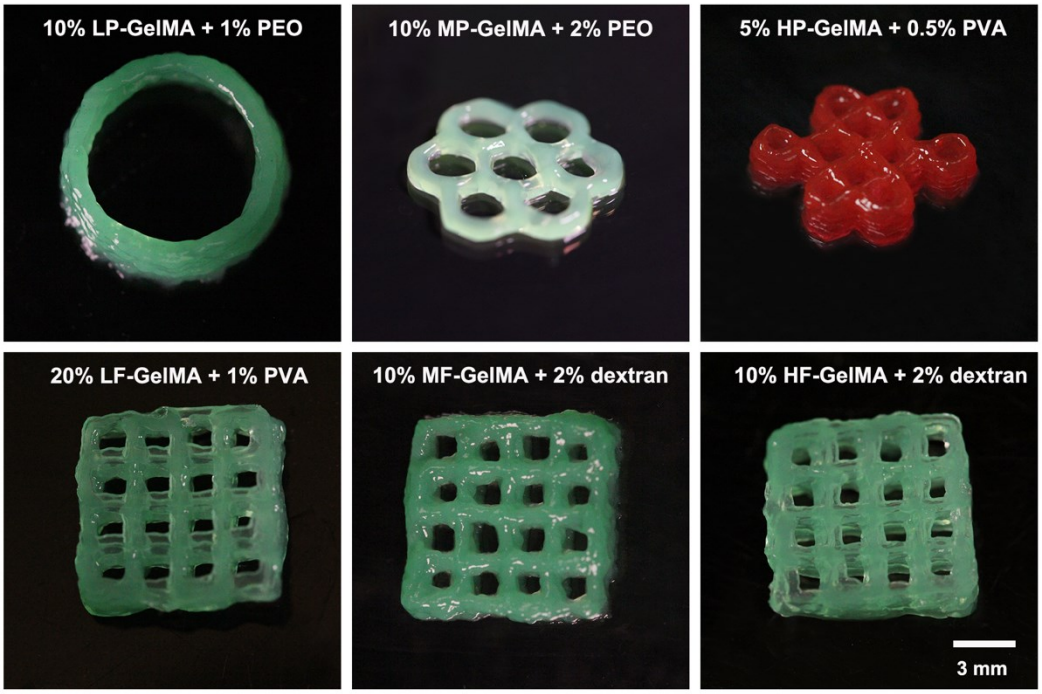

Figure S13. Photographs showing bioprinted multilayered hierarchically microporous GelMA hydrogel patterns using different compositions of the micropore-forming bioinks. PEO (MW: 3×10^5 Da); PVA (MW: 1×10^5 Da); dextran (MW: 5×10^5 Da).

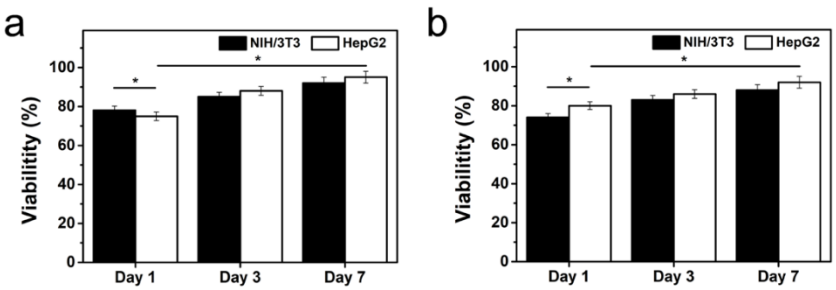

Figure S14. a) Quantification of viability of NIH/3T3 fibroblasts and HepG2 cells within the microporous HF-GelMA (10 wt.%) hydrogel scaffolds made with PVA (1 wt.%, MW: 1×10^5 Da) as the porogen and prepared by extrusion bioprinting at various time points during culture for up to 7 days. (b) Quantification of viability of NIH/3T3 fibroblasts and HepG2 cells within the microporous HF-GelMA (10 wt.%) hydrogel scaffolds made with dextran (2 wt.%, MW: 5×10^5 Da) as the porogen and prepared by DLP bioprinting at various time points during culture for up to 7 days. (*$p<0.05$, n=3)

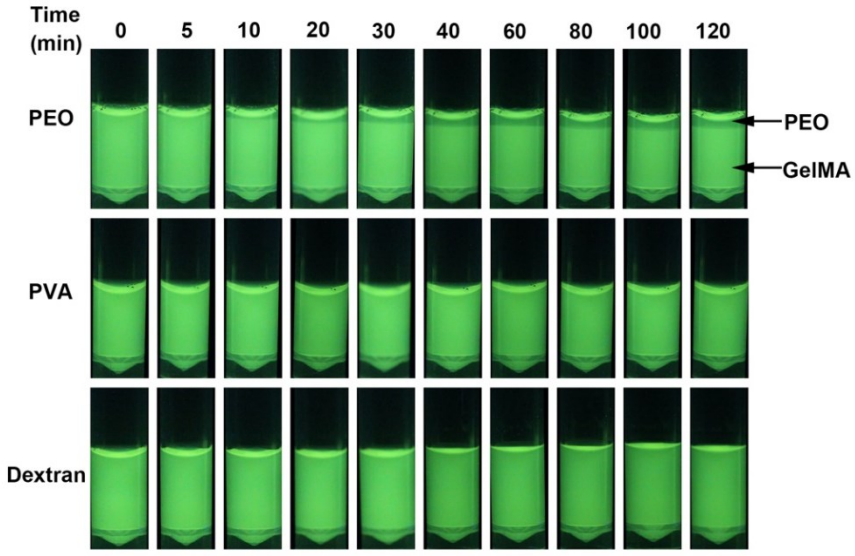

Figure S15. Photographs showing phase separation of the micropore-forming HF-GelMA (10 wt.%; GelMA conjugated with fluorescence) bioinks made with different porogens (1 wt.% and MW: 1×10^5 Da for PEO; 2 wt.% and MW: 1×10^5 Da for both PVA and dextran). The mixtures were kept stationary at the room temperature for up to 120 min.

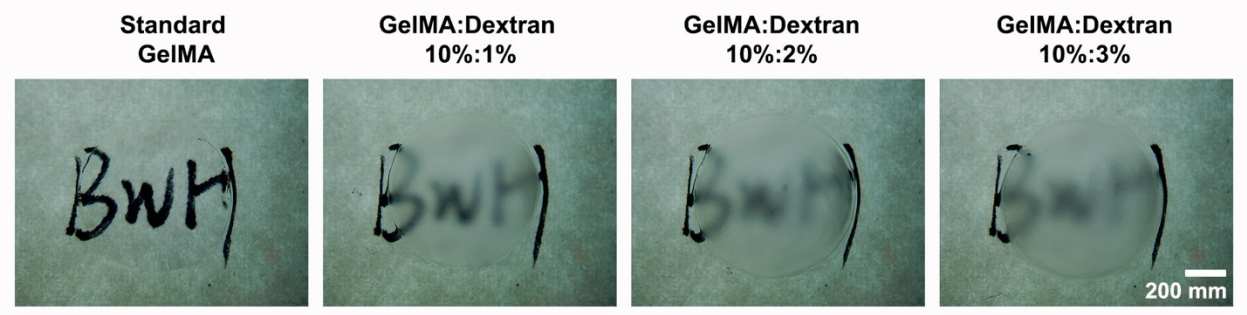

Figure S16. Photographs showing thin pieces HF-GelMA hydrogels with varying dextran (MW: 1×10^5 Da) concentrations, where increased opacity was observed with elevated concentration of dextran.

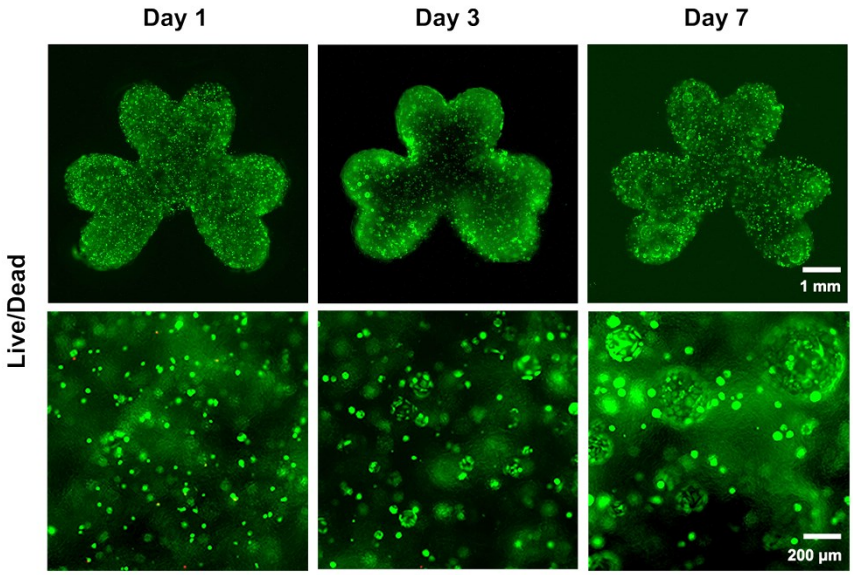

Figure S17. Fluorescence micrographs showing viability of encapsulated HepG2 cells on Days 1, 3, and 7 post-DLP bioprinting, where live cells were stained in green and dead cells in red.

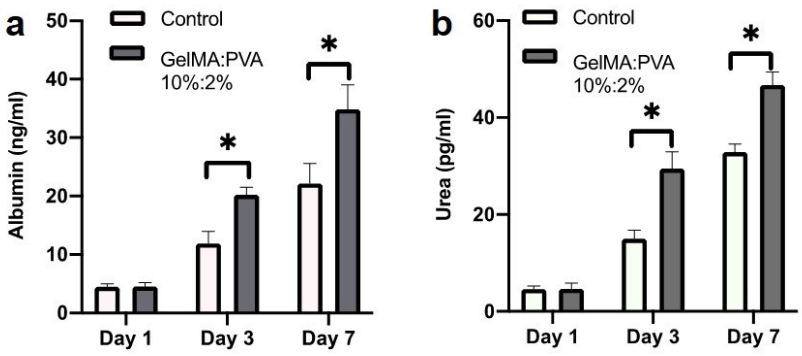

Figure S18. Quantified albumin and urea secretion levels of HepG2 cells cultured in DLP-bioprinted control and microporous GelMA hydrogels during the 7-day culture period. (*$p<0.05$, n=3)

Video S1. Confocal fluorescence reconstruction showing HepG2 cells grown in the microporous HF-GelMA (10 wt.%) hydrogel made with PVA (2 wt.%, M_w: 1×10^5 Da) as the porogen at Day 7. Red: F-actin; blue: nuclei.